

On the properties of the interstellar medium in extremely metal-poor blue compact dwarf galaxies. A VIMOS-IFU study of the cometary galaxy and Ly α absorber Tol 65.*

P. Lagos¹†, R. Demarco², P. Papaderos¹, E. Telles³, A. Nigoche-Netro⁴,
A. Humphrey¹, N. Roche¹ and J. M. Gomes¹

¹*Instituto de Astrofísica e Ciências do Espaço, Universidade do Porto, CAUP, Rua das Estrelas, 4150-762 Porto, Portugal*

²*Department of Astronomy, Universidad de Concepción, Casilla 160-C, Concepción, Chile*

³*Observatório Nacional, Rua José Cristino, 77, Rio de Janeiro, 20921-400, Brazil*

⁴*Instituto de Astronomía y Meteorología, Av. Vallarta 2602. Col. Arcos Vallarta. Guadalajara, Jalisco. C.P. 44130, México*

Accepted 1988 December 15. Received 1988 December 14; in original form 1988 October 11

ABSTRACT

In this study we present high-resolution Visible Multi-Object Spectrograph integral field unit spectroscopy (VIMOS-IFU) of the extremely metal-poor H II/blue compact dwarf (BCD) galaxy Tol 65. The optical appearance of this galaxy shows clearly a cometary morphology with a bright main body and an extended and diffuse stellar tail. We focus on the detection of metallicity gradients or inhomogeneities as expected if the ongoing star-formation activity is sustained by the infall/accretion of metal-poor gas. No evidences of significant spatial variations of abundances were found within our uncertainties. However, our findings show a slight anticorrelation between gas metallicity and star-formation rate at spaxel scales, in the sense that high star-formation is found in regions of low-metallicity, but the scatter in this relation indicates that the metals are almost fully diluted. Our observations show the presence of extended H α emission in the stellar tail of the galaxy. We estimated that the mass of the ionized gas in the tail $M(\text{H II})_{\text{tail}} \sim 1.7 \times 10^5 M_{\odot}$ corresponds with ~ 24 per cent of the total mass of the ionized gas in the galaxy. We found that the H α velocity dispersion of the main body and the tail of the galaxy are comparable with the one found in the neutral gas by previous studies. This suggests that the ionized gas still retains the kinematic memory of its parental cloud and likely a common origin. Finally, we suggest that the infall/accretion of cold gas from the outskirts of the galaxy and/or minor merger/interaction may have produced the almost flat abundance gradient and the cometary morphology in Tol 65.

Key words: galaxies: dwarf – galaxies: individual: Tol 65 (Tol 1223-359, ESO380-G027) – galaxies: ISM – galaxies: abundances.

1 INTRODUCTION

It is well established that interactions and/or galaxy collisions represent an important stage in the evolution of galaxies (e.g. Toomre 1977; Sanders et al. 1988; Springel 2000; Duc et al. 2011). Numerous studies show clear indications of the importance of those external mechanisms for the enhancement of star-formation and its effects in the chemical enrichment of galaxies. In particular, in major merger of massive galaxies the preexisting gas metallicity can be

substantially diluted by the inflow of metal poor gas from the outskirts to the nucleus (e.g. Rupke, Kewley & Barnes 2010; Rich et al. 2012). In the case of low-mass, low-metallicity ($7.0 \leq 12 + \log(\text{O}/\text{H}) \leq 8.4$; Kunth & Sargent 1983) and star-forming dwarf galaxies the effects of tidal interactions and/or mergers (e.g. Bekki 2008; Verbeke et al. 2014) also has a huge impact in their evolution. Observational evidences suggest that H II/BCD galaxies arise from the interactions or accretion of extended H I cloud complexes (e.g. Taylor, Brinks & Skillman 1993; Pustilnik et al. 2001; Ekta, Chengalur & Pustilnik 2008; Ekta & Chengalur 2010a). However, the triggering mechanisms of the current burst of star-formation in those objects is not yet clear since most are, apparently, isolated systems (e.g.

* Based on observations made with ESO Telescopes at the La Silla Paranal Observatory under programme 090.B-0242

† E-mail: plagos@astro.up.pt

Telles & Terlevich 1995; Telles & Maddox 2000). Thus, if not triggered by external agents star-formation is likely produced by internal processes (e.g. gravitational cloud collapse, infall of gas in conjunction with small perturbations) and/or minor mergers (see Lagos et al. 2011, and references therein).

As described above, a considerable fraction of these galaxies has been associated with H I clouds (Taylor, Brinks & Skillman 1993) or low-mass and undetected companions in the optical (e.g. Ekta, Chengalur & Pustilnik 2008), which could rule out the idea of BCD galaxies as isolated systems (Noeske et al. 2001). In fact, a significant fraction of BCDs do show signs of extensions or tails in their outer envelopes, suggesting a tidal origin. Many of these low-metallicity galaxies that show “cometary” or elongated shapes show values of $12+\log(\text{O}/\text{H}) < 7.6$ (e.g. Papaderos et al. 2008). Within this subsample of BCDs or extremely metal poor (XMP) BCD galaxies we found the least chemically evolved galaxies in the local Universe (Kunth & Östlin 2000). This particular morphology has been interpreted for high redshift galaxies in the Hubble Deep Field as the result of weak tidal interactions (Straughn et al. 2006), gravitational instabilities in gas-rich and turbulent galactic disks in formation at high redshift (Bournaud & Elmegreen 2009) and stream-driven accretion of metal-poor gas from the cosmic web (Dekel & Birnboim 2006; Dekel et al. 2009). Papaderos et al. (2008) argue that weak interactions between low-mass stellar or gaseous companions, or propagating shock waves, lead to a bar-like gas distribution triggering the star-formation that by propagation could subsequently produce a cometary morphology in XMP BCDs.

Recently, Sánchez Almeida et al. (2013, 2014a) interpret the metallicity variation in a sample of low metallicity galaxies with cometary morphology as a sign of external gas accretion/infall of metal poor gas. They argue that these results are consistent with the local “tadpole” galaxies being disks in early stages of assembling, with their star-formation sustained by pristine gas infall. In any case, dwarf galaxies tend to show flat abundance (O/H, N/O) gradients (e.g. Kobulnicky & Skillman 1997, 1998; Lee & Skillman 2004; Lagos et al. 2009, 2012), suggesting efficient dispersion and mixing of metals in the interstellar medium (ISM) by expanding starburst-driven superbubbles (e.g. Tenorio-Tagle 1996), afterward the gas begins to cool down by radiation and gravity, and/or external gas infall (e.g. Pérez-Montero et al. 2011; Lagos et al. 2012). These mechanisms have been put forth as potential causes for the observed flat metal distributions in local dwarf galaxies. While in massive star-forming and/or interacting galaxies, bar-induced rotation or shear (e.g. Roy & Kunth 1995) and merger-induced gas flows (e.g. Rupke, Kewley & Barnes 2010) could produce the metal dispersal and mixing. As expressed above, local H II/BCD and XMP BCD galaxies are considered chemically homogeneous and only in a few isolated cases we observed indications of variation of $12+\log(\text{O}/\text{H})$ over the ISM (e.g. SBS 0335-052E, Haro 11, HS 2236+1344; Izotov et al. 1997, 2006; Guseva et al. 2012; Lagos et al. 2014).

In addition to the expected low metal content in young galaxies at high redshift, according to theoretical models

these objects should produce strong Ly α (1216 Å) emission as the result of their intense star-formation activity (e.g. Partridge & Peebles 1967; Charlot & Fall 1993). However, the absence and/or diminished Ly α emission in these galaxies, which is significantly lower than the theoretical recombination ratio, indicate that the Ly α photons are likely redistributed by multiple scattering in the H I envelope, or are absorbed by dust. Examples of the detection of Ly α halos produced by H I scattering envelopes can be seen in the literature (e.g. Humphrey et al. 2013; Guaita et al. 2015). It has been suggested in the literature (e.g. Atek et al. 2008) that there should be an increase in the Ly α /H β flux ratio as the metallicity of the galaxy decreases, since presumably low-metallicity objects contain less dust and hence suffer less Ly α photon destruction. Ly α can also be enhanced at low gas metallicity due to collisional excitation (Villar-Martín et al. 2007). As pointed by Izotov et al. (2004), the fact that there is no Ly α emission in the two most metal-deficient BCDs known, I Zw 18 (Kunth et al. 1994) and SBS 0335-052 (Thuan, Izotov & Lipovetsky 1997), and also in Tol 65, argues against the existence of some correlation between the Ly α emission, metallicity and dust (Giavalisco, Koratkar & Calzetti 1996; Lequeux et al. 1995). Therefore, an important issue in the understanding of Ly α emission in galaxies is the study of the spatial distribution of properties in the ISM of those objects in order to see the different regulation mechanisms involved in the detectability of Ly α emission.

Although during the last years some progress has been made in this field, many questions remain about the metal content, the mechanism involved in the transport and mixing of metals and the star-formation activity in H II/BCD and XMP galaxies. The morphologically diverse nature of H II/BCD, and XMP BCDs, galaxies allows us to consider the role played by galaxy interactions and the feedback between the star-formation and the ISM in the observed metal distributions. Our main objective in this paper is to carry out a spatial investigation of the warm gas properties in the “cometary” and Ly α absorbing XMP H II/BCD galaxy Tol 65. These include, the spatial distribution of emission lines, equivalent width EW(H β), extinction $c(\text{H}\beta)$, ionization ratios ($[\text{O III}]\lambda 5007/\text{H}\beta$, $[\text{S II}]\lambda\lambda 6717, 6731/\text{H}\alpha$ and $[\text{N II}]\lambda 6584/\text{H}\alpha$), kinematics, the chemical pattern (e.g. O/H, N/H and N/O, etc.) and also the possible dependence between these properties. Our aim is to search for the existence of metallicity inhomogeneities as expected if the ongoing star-formation activity is sustained by the infall or accretion of metal-poor gas. To this end, we use high resolution integral field unit (IFU) spectroscopy observations.

The paper is organized as follows: Sect. 2 describes the most important properties of our analyzed galaxy. Sect. 3 contains the technical details regarding observations and the data reduction. Sect. 4 describes our results: the ionized gas structure as well as the physical and kinematic properties of the ionized gas. Sect. 5 discusses the results. Finally, Sect. 6 itemizes the conclusions.

2 OVERVIEW OF TOL 65

Tol 65 is one of the most metal-deficient BCD galaxies known. Izotov et al. (2004) derived a low oxygen abundance

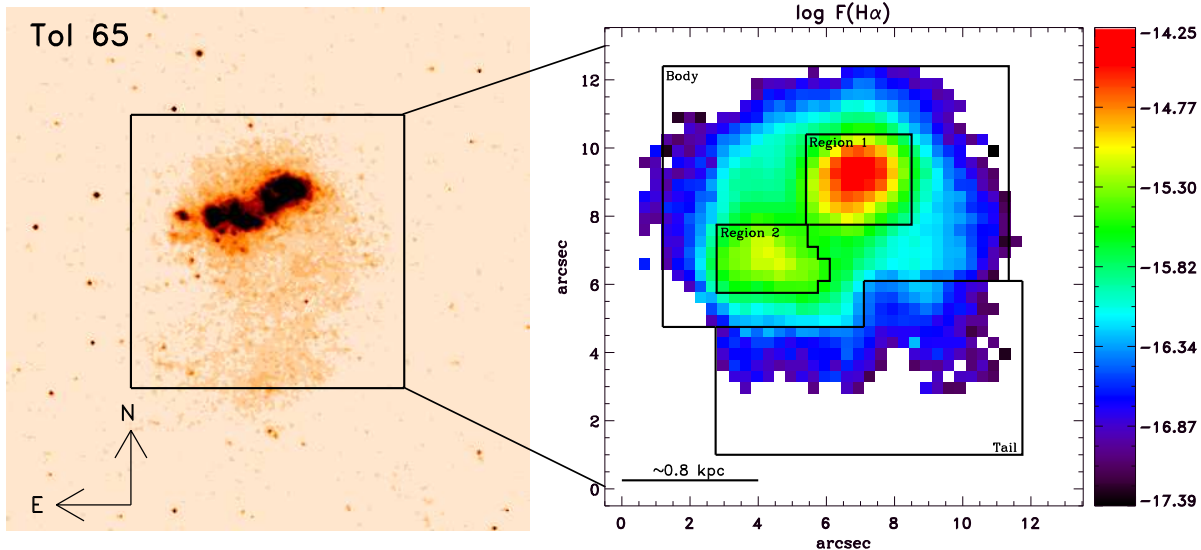


Figure 1. HST image of Tol 65 in the filter F435W (left-hand panel). H α emission line map, in log, of the galaxy (right-hand panel). The VIMOS-IFU FoV of $13'' \times 13''$ (~ 2691 pc \times 2691 pc) is shown over the images. Fluxes are in units of $\text{ergs cm}^{-2} \text{s}^{-1}$.

Table 1. General parameters of Tol 65.

Parameter	Value	Reference
Other names	Tol 1223-359 ESO380-G027	
RA (J2000)	$12^{\text{h}}25^{\text{m}}46.9^{\text{s}}$	
DEC (J2000)	$-36^{\circ}14^{\text{m}}1^{\text{s}}$	
Distance (Mpc)	42.7	Obtained from NED
Pixel scale (pc/arcsec)	207	Obtained from NED
z	0.00936008	Derived from the present observations
$c(\text{H}\beta)$	0.29	Derived from the present observations
$12 + \log(\text{O}/\text{H})$	7.56 ± 0.06	Derived from the present observations
$\log M_{\text{HI}} (M_{\odot})$	8.82	Smoker et al. (2000), Pustilnik & Martin (2007)
$N(\text{HI}) (\text{cm}^{-2})$	$(2.5 \pm 1.0) \times 10^{21}$	Thuan & Izotov (1997)

of $12 + \log(\text{O}/\text{H}) = 7.54 \pm 0.01$, while from the present observations we have obtained a value of $12 + \log(\text{O}/\text{H}) = 7.56 \pm 0.06$. The Nitrogen-to-oxygen ratio $\log(\text{N}/\text{O}) = -1.60 \pm 0.02$ obtained by Izotov et al. appears to be in agreement with the observed value in other XMP BCD galaxies. The optical appearance of this galaxy (see left-hand panel in Fig. 1) shows a clear cometary shape with a bright main body and an extended and diffuse stellar tail (see also Fig. 4 in Lagos et al. 2007). Therefore, Tol 65 is classified as a iL,C according to the Loose & Thuan (1986) classification scheme. Narrow band images (e.g. H β ; Lagos et al. 2007) show that the main body of the galaxy is composed of two Giant HII regions (GHIIRs), or star cluster complexes, while Very Large Telescope (VLT) (Papaderos et al. 1999) and Hubble Space Telescope (HST) images of the same galaxy (left-hand panel of Fig. 1) show that these GHIIRs are formed by several star clusters. The age of the underlying stellar component inferred from radially averaged colour profiles, assuming an instantaneous burst, by Papaderos et al. (1999) and Noeske et al. (2003) is of the order of 10^8 yr.

Thuan & Izotov (1997) showed that the spectrum of this galaxy shows a broad absorption-damped Ly α profile similar to the most metal poor galaxies known in the local Universe: I Zw18 (Kunth et al. 1994) and SBS 0335-052 (Thuan & Izotov 1997). Atek et al. (2008) argue that the young age of Tol 65 (~ 3 Myr) is consistent with a young starburst embedded in a static HI cloud, which produces a damped absorption. Narrow band Ly α imaging of this galaxy, from the same study, show a diffuse Ly α morphology consistent with strong absorption/scattering of Ly α photons by HI. The basic characteristics of the galaxy are compiled in Table 1.

3 OBSERVATIONS AND DATA REDUCTION

The data have been obtained in service mode with the IFU mode of the Visible Multi-Object Spectrograph (VIMOS), hereafter VIMOS-IFU, at ESO mounted on the 8.2 m VLT UT3/Melipal telescope at the Paranal Observatory in Chile.

The VIMOS-IFU array is composed by 4 quadrants and covered by 1600 fibres. We used the scale on the sky of $0.33''$ per fiber covering a Field of View (FoV) of $13'' \times 13''$. We used the high-resolution blue (HR-blue; $0.71 \text{ \AA pixel}^{-1}$) and orange (HR-orange; $0.62 \text{ \AA pixel}^{-1}$) spectral setups, offering a spectral resolving power $R=1440$ between $\sim 3755\text{--}5346 \text{ \AA}$ and $R=2650$ between $\sim 5244\text{--}7440 \text{ \AA}$, respectively. One Arc-line and three flat-field calibration frames were taken for every observing block (OB). The observing log can be found in Table 2. The data reduction was carried out using the *esorex* software version 3.10.2. This includes bias subtraction, flat-field correction, wavelength calibration and flux calibration. The flux calibration was done using observations of spectrophotometric standards included in the standard VIMOS calibration plan. Sky subtraction can be a problem with the VIMOS-IFU, as there are no sky-dedicated fibres. We obtained a night sky spectra from a third exposure, within each set of OB, dithered by $+0.00''$ in RA and by $+0.48''$ in DEC. Therefore, the sky subtraction was performed by averaging the spectra recorded by the sky fibres and subtracting this spectrum from that of each spaxel in the VIMOS-IFU exposures. The data cubes obtained using the gratings HR-orange and HR-blue were shifted and combined, using a sigma-clipping algorithm to remove the cosmic rays, forming a final data cube covering a total spectral range from ~ 3755 to $\sim 7480 \text{ \AA}$. We correct for the quadrant-to-quadrant intensity differences following the procedure applied by Lagerholm et al. (2012) assuming that the intensity correction is uniform within each quadrant. Therefore, we re-normalized the quadrants by comparing the intensity levels of the neighbouring pixels at the quadrant borders and taking a first-order gradient in intensity across the borders into account. When comparing the mean intensity value in quadrants Q1, Q3, and Q4 with respect to quadrant Q2 we found a value of ~ 0.2 , 0.7 and 0.3 , respectively. We checked the effects of the atmospheric refraction (DAR) in each one of our data cubes using an IRAF-based script (Walsh & Roy 1990), but there is no evidence for significant DAR in our data.

Finally, the emission line fluxes were measured using the IRAF task *fitprofs* by fitting, spaxel by spaxel, Gaussian profiles. The two main star cluster complexes or GH IIRs, called here regions nos. 1 and 2, and the other apertures considered in this study, the body and tail, are defined in the right-hand panel of Fig. 1. Figure 2 shows the integrated spectra obtained summing up all spaxels of regions nos. 1 and 2, respectively. In this figure we identified the main emission lines detected and used in our study. In Table 3 we show the observed $F(\lambda)$ and corrected emission line fluxes $I(\lambda)$ relative to the $H\beta$ and their errors (see Lagos et al. 2009) multiplied by a factor of 100, for the main body of the galaxy and regions no. 1 and 2, respectively. We also indicate, in this table, the observed flux of the $H\beta$ emission line, the $EW(H\beta)$, and the extinction coefficient $c(H\beta)$ for the aforementioned apertures. The instrumental contribution to the line broadening was obtained by fitting a single Gaussian to isolated arc lines on a wavelength calibrated arc exposure in the HR-orange observations. Thus, we found the resolution to be $FWHM=1.91 \text{ \AA}$ ($\sim 87.48 \text{ km s}^{-1}$) near $H\alpha$.

Table 2. Observing log.

Grating	OB	Date	Exp. time (s)	Airmass ^a	Seeing ^b
HRO	1	2012-12-28	2×932	1.70-1.57	0.63
	2	2013-12-28		1.38-1.31	1.05
	3	2013-01-21		1.06-1.04	1.03
HRB	1	2013-03-15		1.35-1.43	1.56
	2	2013-04-04		1.04-1.03	0.89
	3	2013-04-04		1.02-1.02	0.89

^a Mean value at start of exposures and at end of exposures

^b Mean value during the observation

4 RESULTS

4.1 Emission lines, $EW(H\beta)$, extinction and emission line ratio maps

The peak of $H\alpha$ emission is placed on the designated region no. 1 while faint $H\alpha$ emission is detected over the stellar tail of the galaxy. This structure is visible more easily in the lower panel of Fig. 10. We will present this Fig. below in Sect. 4.4. The recombination lines ($H\beta$, $H\gamma$, etc.) and the forbidden emission lines $[O III]\lambda 5007$, $[O III]\lambda 4363$, $[S II]\lambda\lambda 6712, 6731$, $[N II]\lambda 6584$, etc. displays very similar spatial morphology to that of $H\alpha$ in Fig. 1.

The $H\beta$ equivalent width, $EW(H\beta)$, map of the galaxy in Fig. 3 (left-hand panel) ranges values from $\sim 3 \text{ \AA}$ to 297 \AA , with the highest values located at the two star-forming regions. This map resembles that obtained by Lagos et al. (2007), it to say, the peak of the $EW(H\beta)$ and $H\alpha$ emission of the galaxy are almost coincident. Although the observed $EW(H\beta)$ can be affected by the contribution to the continuum by the accumulation of old populations of stars from previous bursts, multiplicity of the star-forming knots into several individual star clusters (Lagos et al. 2007), and the leaking of ionizing photons (see Papaderos et al. 2013, and references therein), its value can be understood as an age indicator (Dottori 1981; Copetti, Pastoriza & Dottori 1986), with $EW(H\beta)$ values decreasing with the age of the starburst. Hence, a crude estimation of the age of the current burst of star-formation can be obtained by using the integrated $EW(H\beta)$ in each of the regions. Therefore, we use the same SSP models from STARBURST99 (Leitherer et al. 1999) as in Lagos et al. (2014) in order to obtain a rough idea of the age of the current burst of star-formation in the GH IIRs of the galaxy. From the integrated spectrum of the body of the galaxy one infers, for an instantaneous burst, an upper limit to the age of 4.26 Myr (~ 4 Myr) and 2.91 Myr (~ 3 Myr) and 4.95 Myr (~ 5 Myr) for regions nos. 1 and 2, respectively. The aforementioned effects themselves represent an important source of uncertainty in the determination of absolute ages and also it may be highly model dependent. However, those results are indicative of a young burst and are only provided for the sake of comparison with previous studies (e.g. Atek et al. 2008).

The reddening coefficient $c(H\beta)$ was determined from the comparison of the observed flux ratio of the Balmer $H\alpha$ and $H\beta$ and the theoretical line ratio computed by Osterbrock & Ferland (2006) for the physical conditions of

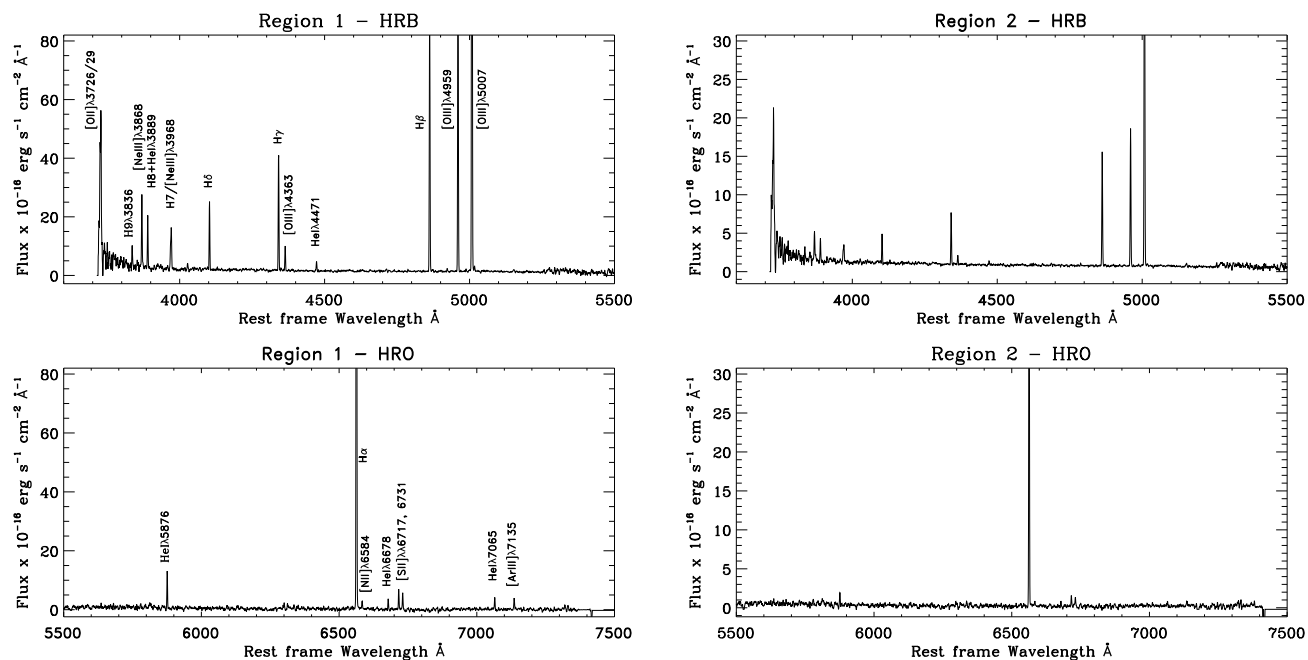


Figure 2. Tol 65. Integrated HR-blue (upper panel) and HR-orange (lower panel) spectrum of the two GH IIRs resolved in the galaxy. The most important emission lines are labelled in the panels.

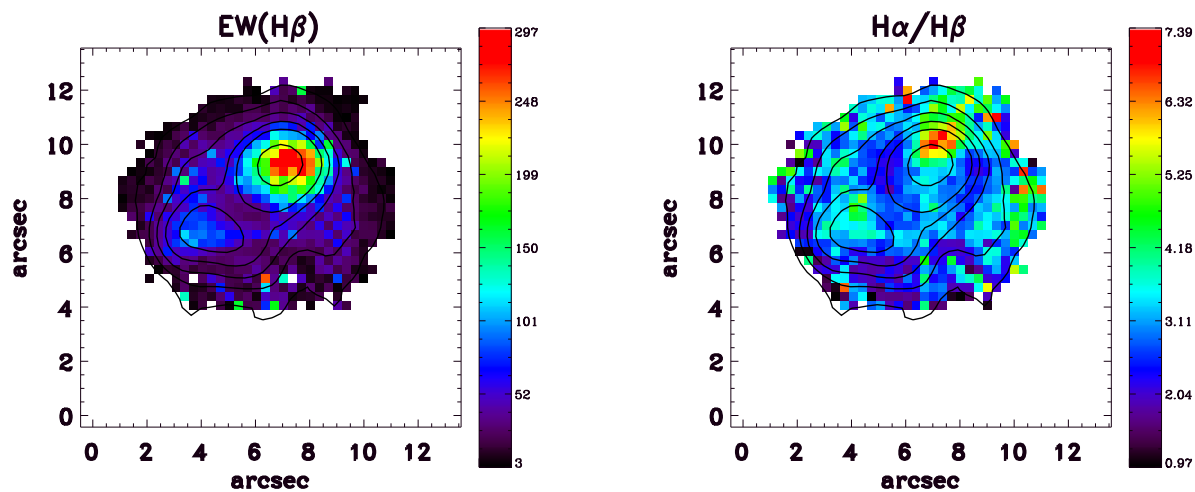


Figure 3. Right-hand panel: Spatial distribution of the $H\alpha/H\beta$ emission line ratio. Left-hand panel: $H\beta$ equivalent width map of the galaxy. $EW(H\beta)$ is in units of \AA . The $H\alpha$ emission line contours are overlaid in the panels. North is up and east is to the left.

the nebula assuming case B at $T=2\times 10^4$ K. We used the reddening function $f(\lambda)$ derived by Cardelli, Clayton & Mathis (1989) and assuming $R_V = 3.1$. Figure 3 (right-hand panel) shows the spatial distribution of the $H\alpha/H\beta$ emission line ratio. The $c(H\beta)$ value obtained in this study is 0.29 ± 0.05 for the main body and 0.40 ± 0.02 and 0.29 ± 0.06 for regions nos. 1 and 2, respectively. Our values are similar, within the uncertainties, to the ones obtained by Guseva et al. (2011) for their individual regions with values of 0.285 ± 0.018 and 0.180 ± 0.019 , respectively. The $c(H\beta)$ distribution as seen by the $H\alpha/H\beta$ map does not resemble the structure of the dust content in the extinction, $E(B-V)$, map of Tol 65 presented by Atek et al. (2008). Our spatial distribution shows

the maximum values displaced from the peak of $H\alpha$ line emission, while the one presented by Atek et al. (2008) appears similar to the $H\alpha$ emission line distribution.

To infer the dominant ionization source in the gas at spaxel scales we employ the commonly used diagnostic or BPT (Baldwin, Phillips & Terlevich 1981) diagrams on the basis of the following emission-line ratios: $[O III]\lambda 5007/H\beta$, $[S II]\lambda\lambda 6717, 6731/H\alpha$ and $[N II]\lambda 6582/H\alpha$. In Figure 4 we show those emission-line-ratio maps. The spatial structure of those maps changes from the peak of $H\alpha$ emission, in each one of the regions, to the outer part of the galaxy. Meanwhile the ionization structure on the GH IIRs is rather constant for all emission line ratios. All points fall, in Fig. 4,

in the locus predicted by models of photo-ionization (we will not show the BPT diagrams in this study) by young stars in H II regions (Osterbrock & Ferland 2006) corroborating that photoionization from stellar sources is the dominant excitation mechanism in Tol 65.

We found a weak He II $\lambda 4686$ emission in both regions of the galaxy (we will not show the spectra in this study). It shows the same shapes as the spectra showed by Izotov et al. (2004) in their fig. 3 and 4, but the low S/N=signal-to-noise (S/N) ratio < 3 in these regions does not allow us an adequate study of the spatial morphology of this emission line. However, we note that the peak of H α and He II $\lambda 4686$ are coincident, so we can associate the spatial distribution of He II $\lambda 4686$, in Tol 65, with current sites of star-formation activity. Given the very young age of the starburst ~ 3 -5 Myr the presence of Wolf-Rayet (WR) stars is expected. Since the population of WRs decreases with metallicity (Cerviño & Mas-Hesse 1994) and the detection of WR features depends on the quality of the spectra, location through the galaxy and size of the apertures, the stellar feature of WR stars are not observed in the spectra of Tol 65. In any case, the lack of detection of WR features in this galaxy does not exclude the presence of these stars.

Finally, as a check on the results we compare our spectrophotometric values with those obtained using narrow-band H β images by Lagos et al. (2007). In Lagos et al. (2007) we found a $F(H\beta)$ of 6.91×10^{-14} erg s $^{-1}$ cm $^{-2}$ for the main body of the galaxy and 3.47×10^{-14} erg s $^{-1}$ cm $^{-2}$ and 0.41×10^{-14} erg s $^{-1}$ cm $^{-2}$ for regions nos. 1 and 2, respectively. While the EW(H β), in that study, reaches values of 157 Å, 287 Å and 86 Å for the same apertures. Our results agree very well with the aforementioned study with an average difference of ~ 30 per cent for H β fluxes and ~ 22 per cent for EW(H β). Our integrated $F(H\alpha)$ flux, in the body of the galaxy, differ ~ 35 per cent with that obtained by Gil de Paz, Madore & Pevunova (2003) from Narrow-band H α images. These differences are perfectly explained by the uncertainties associated with measurements and the different sizes adopted for the apertures. However, the flux calibration accuracy has little effect on the analysis of the internal physical conditions of this one object.

4.2 Chemical abundances

4.2.1 Electron temperature and density

The first step in the abundance derivation is to obtain the electron density and temperature. The $[O III]\lambda\lambda 4959, 5007/[O III]\lambda 4363$ intensity ratio was used to determine the electron temperature $t_e(O III)$ and the electron density $n_e(S II)$ was obtained from the emission line doublet $[S II]\lambda 6716/[S II]\lambda 6731$ ratio. We computed the values of $t_e(O III)$ and $n_e(S II)$ using the IRAF STS package *nebular*.

Figure 5 shows the spatial distribution of electron temperature $t_e(O III)$ (left-hand panel) and density $n_e(S II)$ (right-hand panel) of Tol 65. The range of valid data points for the $t_e(O III)$ varies from 0.89 to $\sim 2.9 \times 10^4$ K, while the electron density range from ~ 67 cm $^{-3}$ to ~ 1000 cm $^{-3}$. We note that the ratio $[S II]\lambda 6717/[S II]\lambda 6731$ is typically greater than 1 and only a few spaxels show values ~ 1000 cm $^{-3}$, which indicates a dominant low den-

sity regime (Osterbrock & Ferland 2006) in the ISM of the galaxy, hence we assumed an electron density of $n_e \sim 100$ cm $^{-3}$ for those apertures in our calculations. Aperture regions nos. 1 and 2 show temperatures of 18587 ± 335 and 17152 ± 715 K, while $n_e(S II)$ shows values of 212 cm $^{-3}$ and 100 cm $^{-3}$, respectively. The $t_e(O III)$ and $n_e(S II)$ found in this study agree, within the uncertainties, with the ones obtained by Izotov et al. (2004) and Guseva et al. (2011) derived from their high and medium-resolution spectra.

4.2.2 Abundances determination

Oxygen, nitrogen, neon, sulfur and argon abundances were calculated using the five level atomic model FIVEL (De Robertis, Dufour & Hunt 1987) implemented in the IRAF STS package *nebular* (*abund*; Shaw & Dufour 1994) using the $t_e(O III)$ and $n_e(S II)$ obtained previously in Sect. 4.2.1 and assuming that: $\frac{O}{H} = \frac{O^+}{H^+} + \frac{O^{+2}}{H^+}$, $\frac{N}{H} = ICF(N) \frac{N^+}{H^+}$, $\frac{Ne}{H} = ICF(Ne) \frac{Ne^{+2}}{H^+}$, $\frac{S}{H} = ICF(S) \left(\frac{S^+}{H^+} + \frac{S^{+2}}{H^+} \right)$, and $\frac{Ar}{H} = ICF(Ar) \frac{Ar^{+2}}{H^+}$. Where O $^+$, O $^{+2}$, N $^+$, Ne $^{+2}$, S $^+$ and Ar $^{+2}$ correspond to the ions of the different atomic species, and the ICF to the ionization correction factor, respectively. We used the relationship between S $^+$ and S $^{+2}$ given by Kingsburgh & Barlow (1994), assuming an $ICF(Ar)=1.87$ and that the $t_e(O II)$ temperature is given by $t_e(O II) = 2/(t_e^{-1}(O III)+0.8)$ (Pagel et al. 1992). In Figure 6 we show the oxygen, nitrogen, neon, argon and sulfur abundance maps and in Fig. 7 we show the $\log(N/O)$, $\log(Ne/O)$, $\log(Ar/O)$ and $\log(S/O)$ ratio maps of Tol 65. Table 4 shows the abundances calculated for the different apertures considered in this study. Below in section 4.2.3 we will describe the distribution of abundances for the different atomic species obtained from the procedures described above.

4.2.3 Elemental abundances and its spatial distribution

- Oxygen: The integrated oxygen abundance of $12+\log(O/H)=7.56 \pm 0.06$, in the body of the galaxy, is in agreement with those provided in the literature, using long-slit, of 7.53 ± 0.05 (Kunth & Sargent 1983), 7.59 ± 0.05 (Pagel et al. 1992), $7.556_{-0.035}^{+0.032}$ (Kunth & Jourbert 1985) and $12+\log(O/H)=7.54 \pm 0.01$ (Izotov et al. 2001, 2004). Both GH IIRs show the same oxygen abundance, within the uncertainties, with values of $12+\log(O/H)=7.54 \pm 0.04$ and 7.58 ± 0.08 , respectively. The $12+\log(O/H)$ values, in Fig. 6, range from 7.38 to 7.99 showing an almost constant pattern over the GH IIRs. However, we found that the maximum values of oxygen are not peaked in the centre part of region no. 1, indicating a slight rising abundance gradient towards the outskirts of this region.

- Nitrogen: We found an integrated value for the body of Tol 65 of $12+\log(N/H)=5.95 \pm 0.13$, and 5.79 ± 0.07 and 5.97 ± 0.18 in regions nos. 1 and 2, respectively. The nitrogen-to-oxygen ratio in the body is $\log(N/O)=-1.61 \pm 0.20$, and -1.75 ± 0.10 and -1.61 ± 0.27 in regions nos. 1 and 2, respectively. Those values agree, within the uncertainties, with those measured by Izotov et al. (2001) of -1.60 ± 0.02 for the integrated galaxy and by Izotov et al. (2004) of -1.595 ± 0.019 and -1.635 ± 0.041 for our regions nos. 1 and 2, respectively. Therefore, the nitrogen abundances of both

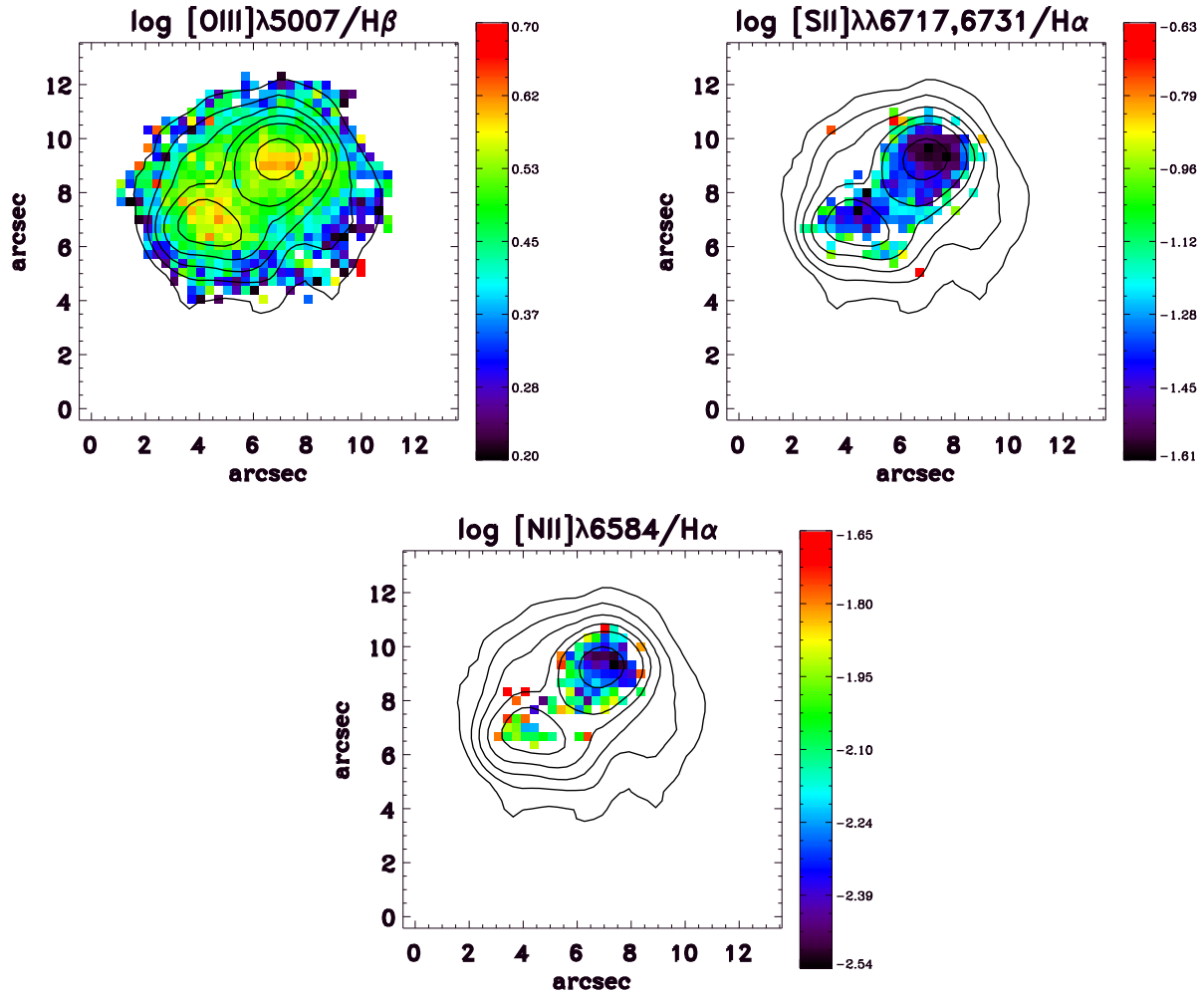


Figure 4. $[O\text{III}]\lambda 5007/H\beta$, $[S\text{II}]\lambda\lambda 6712,6731/H\alpha$ and $[N\text{II}]\lambda 6584/H\alpha$ emission line ratio maps. $H\alpha$ emission line contours are overlaid in the panels. North is up and east is to the left.

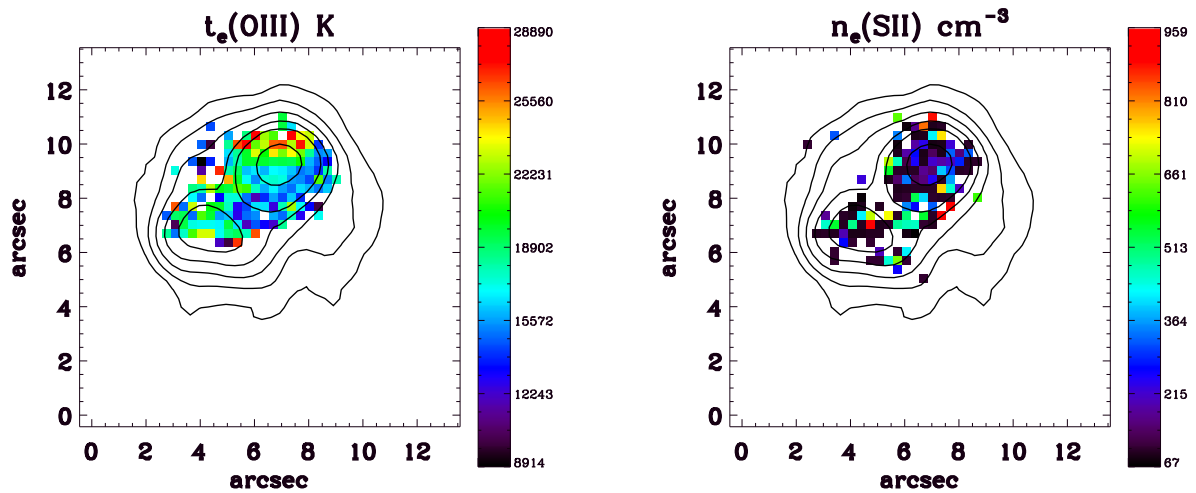


Figure 5. Electron temperature $t_e(O\text{III})$ (left-hand panel) and density $n_e(S\text{II})$ (right-hand panel) maps of Tol 65. $H\alpha$ emission line contours are overlaid in the panel. North is up and east is to the left.

Table 3. Observed and extinction corrected emission lines in Tol 65. The fluxes are relative to $F(\text{H}\beta)=100$.

	Main Body		Region no. 1		Region no. 2	
	$F(\lambda)/F(\text{H}\beta)$	$I(\lambda)/I(\text{H}\beta)$	$F(\lambda)/F(\text{H}\beta)$	$I(\lambda)/I(\text{H}\beta)$	$F(\lambda)/F(\text{H}\beta)$	$I(\lambda)/I(\text{H}\beta)$
[OII] λ 3726	31.55±2.63	39.13±4.61	45.94±7.35	61.82±13.99	21.89±1.48	27.15±2.59
[OII] λ 3729	50.48±6.34	62.58±11.11	46.31±4.41	62.28±8.39	63.79±1.29	79.08±2.26
H9 λ 3836	13.64±2.05	16.65±3.54	7.79±0.40	10.26±0.74	10.76±1.73	13.13±2.98
[NeIII] λ 3868	15.65±3.92	19.01±6.73	23.97±2.94	31.35±5.44	19.09±4.53	23.19±7.78
H8+He I λ 3889	16.87±3.32	20.42±5.68	17.87±1.05	23.26±1.93	16.52±4.46	20.00±7.64
[NeIII] λ 3968	5.48±0.94	6.55±1.59	8.64±0.22	11.04±0.40	8.88±0.87	10.61±1.47
H7 λ 3970	17.49±5.58	20.89±9.42	14.77±3.42	18.87±6.18	21.26±5.23	25.39±8.83
H δ λ 4101	26.48±2.04	30.87±3.36	25.54±1.10	31.56±1.92	26.29±2.14	30.65±3.68
H γ λ 4340	42.80±2.70	47.52±4.24	44.51±1.80	51.41±2.94	42.69±2.59	47.40±4.07
[OIII] λ 4363	7.71±0.33	8.52±0.51	9.25±0.21	10.61±0.34	8.11±0.46	8.96±0.72
HeI λ 4471	2.76±0.95	2.98±1.45	3.46±0.66	3.85±1.02	2.82±0.88	3.05±1.34
H β λ 4861	100.00±0.70	100.00±0.99	100.00±0.81	100.00±1.15	100.00±3.37	100.00±4.77
[OIII] λ 4959	118.10±1.89	116.09±2.63	126.94±1.40	123.97±1.93	122.46±2.84	120.38±3.95
[OIII] λ 5007	352.26±5.36	343.49±7.39	377.43±2.63	364.53±3.59	369.05±6.22	359.86±8.58
HeI λ 5876	14.27±2.57	12.46±3.17	13.22±1.24	10.96±1.45	13.95±2.19	12.18±2.70
[OI] λ 6300	2.08±0.23	1.63±0.25
[SIII] λ 6312	1.83±0.34	1.43±0.38
[OI] λ 6363	1.15±0.45	0.89±0.49
H α λ 6563	348.56±6.00	285.75±6.96	377.43±2.63	286.95±2.83	348.63±6.71	285.80±7.78
[NII] λ 6584	3.52±0.80	2.88±0.93	3.29±0.41	2.49±0.44	3.66±0.55	2.99±0.64
HeI λ 6678	11.45±1.60	9.29±1.84	4.83±0.37	3.62±0.39	7.05±0.82	5.72±0.94
[SII] λ 6717	7.16±0.83	5.79±0.95	6.81±0.39	5.08±0.41	7.61±0.96	6.15±1.10
[SII] λ 6731	5.81±0.67	4.69±0.76	5.52±0.13	4.11±0.24	4.71±0.75	3.80±0.86
HeI λ 7065	5.46±0.80	4.28±0.89	4.44±0.58	3.17±0.59	3.25±0.95	2.55±1.05
[ArIII] λ 7136	3.12±0.55	2.43±0.61	3.91±0.33	2.77±0.33	3.79±0.59	2.95±0.65
$F(\text{H}\beta)^a$	45.96±0.16		27.21±0.11		4.75±0.08	
$\text{EW}(\text{H}\beta)^b$	121		257		68	
$c(\text{H}\beta)$	0.29±0.05		0.40±0.02		0.29±0.06	

^a In units of $\times 10^{-15}$ erg cm^{-2} s^{-1} ^b In units of \AA

star-forming regions, and also the main body, are consistent with those of other XMP galaxies in the literature of similar oxygen abundance (see Fig. 13 in Lagos et al. 2014). However, there is a slight correlation between the N/O ratio map in region no. 1 and the O abundance, in the sense that high N/O values are, preferentially, placed in regions of lower oxygen abundance. This is compatible by considering the O/H distribution alone without a need to invoke an N enhancement in the nucleus within the uncertainties.

- Neon, Argon and Sulfur: The Ne/H, Ar/H and S/H distribution across the GH IIRs of Tol 65 are relatively constant, within the uncertainties. We obtained integrated values of $12+\log(\text{Ne}/\text{H})=6.66\pm 0.23$, 6.81 ± 0.12 and 6.74 ± 0.31 , $12+\log(\text{Ar}/\text{H})=5.17\pm 0.05$, 5.17 ± 0.03 and 5.25 ± 0.06 for the body of the galaxy and regions nos. 1 and 2, respectively. For these apertures we found values of $\log(\text{Ne}/\text{O})=-0.90\pm 0.29$, -0.72 ± 0.15 and -0.83 ± 0.39 ; and $\log(\text{Ar}/\text{O})=-2.39\pm 0.11$, -2.37 ± 0.06 and -2.33 ± 0.15 , for the same aforementioned apertures. We derived Sulfur abundances only in region no. 1. Thus, we found values of $12+\log(\text{S}/\text{H})=5.67\pm 0.03$ and $\log(\text{S}/\text{O})=-1.86\pm 0.06$ for that region.

4.2.4 Summary of the results and comparison with other spaxel scale

Figure 8 shows the spatial distribution of the binned ($\sim 1.0''$) $12+\log(\text{O}/\text{H})$ abundances and [S II] $\lambda\lambda$ 6717,6731 profiles. To do this we summed the spaxels, in the data cube, in a region of 3×3 spaxels in order to increase the S/N. From this figure it is clear that the results obtained previously in this Sect. are consistent when we binned the spaxels from the $0.33''$ to $\sim 1.0''$, which corresponds approximately with the mean value of the seeing during the observations. We note in Fig. 8 that the intensity of the central peak of the [S II] λ 6731 emission line is slightly higher than the intensity of [S II] λ 6717 in a few spaxels in between the GH IIRs. This indicate that this area shows high electron density values $\gg 100 \text{ cm}^{-3}$. On the other hand, we did not observe any chemical inhomogeneity, within the uncertainties, along the main body of the galaxy. However, the highest values of $12+\log(\text{O}/\text{H})$ and lowest values of $t_e(\text{O III})$ are placed on the southern part of region no. 1 and following the same pattern found at $0.33''$ spatial scale, while the $12+\log(\text{O}/\text{H})$ for the different apertures considered here are similar. Therefore, the spatial distribution of O, Ne, S, Ar and also N/O, Ne/O, Ar/O and S/O abundances in this XMP H II/BCD appear to be flat at large scales. This result agrees with previous studies in the litera-

Table 4. Ionic, abundances and integrated properties of Tol 65. ICFs are taken from Kingsburgh & Barlow (1994) and assuming ICF(Ar)=1.87.

	Main Body	Region no. 1	Region no. 2
Te(OIII) K	17087±534	18587±336	17152±715
Ne(II) cm ⁻³	100	212	100
O ⁺ /H ⁺ × 10 ⁵	0.98±0.04	1.09±0.02	1.02±0.06
O ⁺⁺ /H ⁺ × 10 ⁵	2.67±0.19	2.35±0.09	2.76±0.26
O/H × 10 ⁵	3.64±0.23	3.44±0.11	3.78±0.32
12+log(O/H)	7.56±0.06	7.54±0.04	7.58±0.08
N ⁺ /H ⁺ × 10 ⁶	0.24±0.01	0.20±0.01	0.25±0.01
ICF(N)	3.73±0.40	3.15±0.18	3.72±0.52
N/H × 10 ⁶	0.90±0.12	0.62±0.04	0.93±0.17
12+log(N/H)	5.95±0.14	5.79±0.07	5.97±0.18
log(N/O)	-1.61±0.20	-1.74±0.10	-1.61±0.27
S ⁺ /H ⁺ × 10 ⁷	...	0.59±0.03	...
S ⁺⁺ /H ⁺ × 10 ⁶	...	0.36±0.02	...
ICF(S)	1.18±0.05	1.14±0.03	1.18±0.06
S/H × 10 ⁶	...	0.47±0.01	...
12+log(S/H)	...	5.67±0.03	...
log(S/O)	...	-1.86±0.06	...
Ne ⁺⁺ /H ⁺ × 10 ⁵	0.33±0.03	0.44±0.02	0.40±0.04
ICF(Ne)	1.37±0.19	1.46±0.11	1.37±0.25
Ne/H × 10 ⁵	0.46±0.10	0.65±0.08	0.55±0.17
12+log(Ne/H)	6.66±0.23	6.81±0.12	6.74±0.31
log(Ne/O)	-0.90±0.29	-0.72±0.15	-0.83±0.40
Ar ⁺⁺ /H ⁺ × 10 ⁷	0.78±0.04	0.79±0.02	0.95±0.06
Ar/H × 10 ⁷	1.47±0.07	1.48±0.04	1.77±0.12
12+log(Ar/H)	5.17±0.05	5.17±0.03	5.25±0.07
log(Ar/O)	-2.39±0.11	-2.37±0.06	-2.33±0.15
log([OIII] λ5007/Hβ)	0.53±0.02	0.56±0.01	0.56±0.02
log([NII] λ6584/Hα)	-1.54±0.34	-1.60±0.18	-1.52±0.21
log([SII] λλ6717,6731/Hα)	-0.98±0.16	-1.04±0.07	-1.00±0.19
σ(Hα) km s ⁻¹	20.8±0.6	19.6±0.6	22.5±0.4

ture (e.g. Lagos et al. 2009, 2012; Lagos & Papaderos 2013, and references therein) in the sense that no spatial variations of oxygen abundance has been found in HII/BCD galaxies. Finally, it is interesting to note that if we assume an electron density of $n_e \sim 100 \text{ cm}^{-3}$ for the individual spaxels we obtain a mean abundance value of 7.50 in units of 12+log(O/H). Meanwhile if we assume a density of 1000 cm^{-3} we obtain that the mean value of 12+log(O/H)=7.63. Therefore, no significant changes in metallicity are found, within the uncertainties, when we assume a constant density of 100 cm^{-3} through the ISM of the galaxy.

4.3 Gas Kinematics

The kinematics distribution of the emitting gas was obtained by fitting Gaussian curves to the line profiles of Hα. The complexity of the internal motions in Tol 65 can be seen in Fig. 9. The radial velocity $V_r(\text{H}\alpha)$ map of the galaxy (left-hand panel) shows no spatial correlation with the Hα emission and we found no evidence of velocity gradients or rotational patterns. Meanwhile, the FWHM(Hα) map (right-hand panel) shows the lowest values on the two star-formation regions. We note that these velocity fields are akin the ones observed in II Zw 40 by Bordalo, Plana & Telles (2009), in the sense that some regions does not seem to play a significant role stirring the gas up, then likely preserving

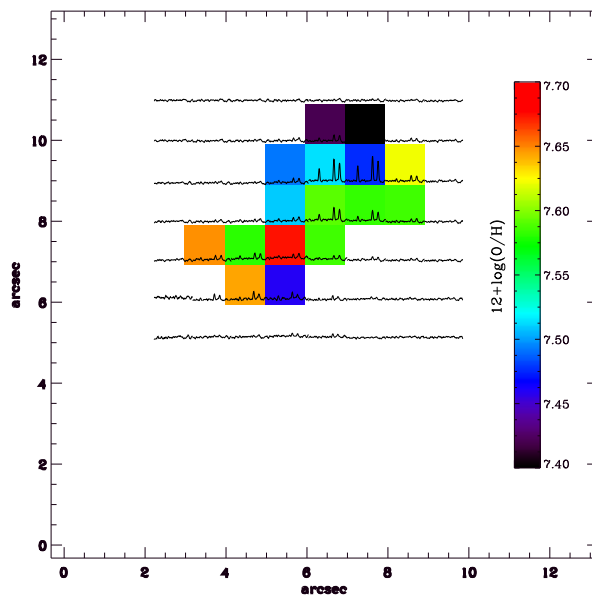


Figure 8. Spatial distribution of the binned ($\sim 1''$ spaxels) 12+log(O/H) abundances and [S II] λλ6717,6731 emission line profiles. North is up and east is to the left.

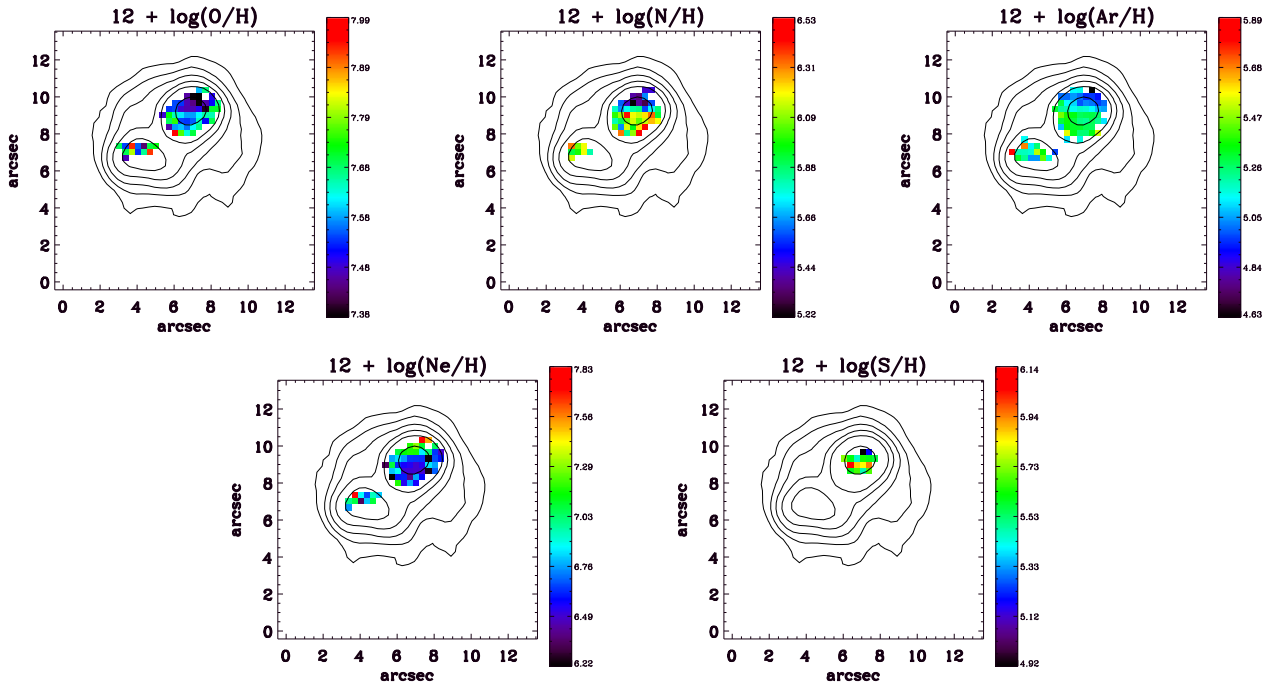


Figure 6. $12+\log(\text{O}/\text{H})$, $12+\log(\text{N}/\text{H})$, $12+\log(\text{Ar}/\text{H})$, $12+\log(\text{N}/\text{H})$ and $12+\log(\text{S}/\text{H})$ abundance maps for Tol 65. $\text{H}\alpha$ emission line contours are overlaid in the panels. North is up and east is to the left.

the kinematic signature of the proto-cloud, while extended regions of the low intensity and diffuse gas are highly disturbed, probably due to unresolved expanding shells and the effects of massive star evolution (i.e., supernovae, champagne flows, relative motions between discrete clusters providing large scale shear, and turbulence and rotation).

Despite the different sizes, the two main regions have the same kinematic properties, with very similar patterns. Both regions have smooth line profiles with $\sigma \sim 19.6 \pm 0.6 \text{ km s}^{-1}$ and $22.5 \pm 0.4 \text{ km s}^{-1}$ and a heliocentric $V_r \sim 2805.51 \text{ km s}^{-1}$ and $2808.03 \text{ km s}^{-1}$, respectively. The velocity dispersion ($\sigma = \text{FWHM}/2.35$) was obtained considering the instrumental dispersion, see Sect. 3, and $\sigma_{th} = \sqrt{kT_e/m_H} \sim 12 \text{ km s}^{-1}$ for the thermal broadening at $t_e(\text{O III}) = 17087 \text{ K}$, thus $\sigma^2 = \sigma_{obs}^2 - \sigma_{inst}^2 - \sigma_{th}^2$. Our corrected velocity dispersion $\sigma(\text{H}\alpha) = 20.8 \pm 0.6 \text{ km s}^{-1}$ for the body of the galaxy agrees with the value obtained by Bordalo & Telles (2011) of $\sigma(\text{H}\alpha) = 18.4 \pm 0.4 \text{ km s}^{-1}$. This is identical, within the errors, to the velocity of the H I cloud with a line width of $w_{50} = 40 \pm 6 \text{ km s}^{-1}$ ($\sigma \sim 17 \text{ km s}^{-1}$) obtained by Pustilnik & Martin (2007). This implies that the ionized gas still retains the kinematic memory of its parental cloud likely to be associated with the gravitational potential well (see Bordalo, Plana & Telles 2009).

It is interesting to note that the zone in between regions nos. 1 and 2, see Fig. 9, shows low $V_r(\text{H}\alpha)$ and high FWHM($\text{H}\alpha$) values. This suggest that the kinematic structure of the galaxy is likely dominated by the current burst of star-formation (e.g. Moiseev, Tikhonov & Klypin 2015). It may indicate a weak outflow seen towards the observer. Therefore, turbulent motions resulting from the starburst appear to dominate over rotation in this galaxy. Moiseev, Tikhonov & Klypin (2015) obtain a similar con-

clusion based in the analysis of a large sample of H II/BCD galaxies obtained using Fabry-Perot interferometry. In addition, we found a velocity dispersion slightly lower in the tail of the galaxy with a value of $\sigma(\text{H}\alpha) = 17.5 \pm 1.0 \text{ km s}^{-1}$. The difficulties in calculating these values and the small difference within them lead us to consider $\sigma_{body} \simeq \sigma_{tail}$. Finally, we did not observe the presence of asymmetric line profiles or/and a broad component in the base of the emission lines. We will discuss in detail in Sect. 5 the results obtained in this section and its implications in the evolutionary stage of the galaxy.

4.4 Mass of the ionized hydrogen in the tail of the galaxy

In the upper panel of Fig. 10 we show the spatial distribution of the binned ($\sim 1''$) $\text{H}\alpha$ emission line profiles, while in the lower panel of the same Fig. we show the integrated spectrum of the tail. In Table 5 we show the fluxes and the extinction obtained in that region. It is clear from Fig. 10 and also Fig. 1 (right-hand panel) that there is an extended nebular emission in the tail of the galaxy. The presence of this extended nebular emission can have a large impact on the inferred properties of the underlying stellar component (e.g. Papaderos & Östlin 2012). According to Duc, Bournaud & Masset et al. (2004) the effect of tidal perturbations can efficiently carry away from the disk a large fraction of the gas. At this point, we can ask if the observed ionized gas in the tail of the galaxy is it the result of a tidal perturbation, infall of gas or merely the consequence of the star-formation activity (see Sect. 5.3).

In this context, an estimate of the mass of emitting ionized hydrogen in the tail of the galaxy, is an important

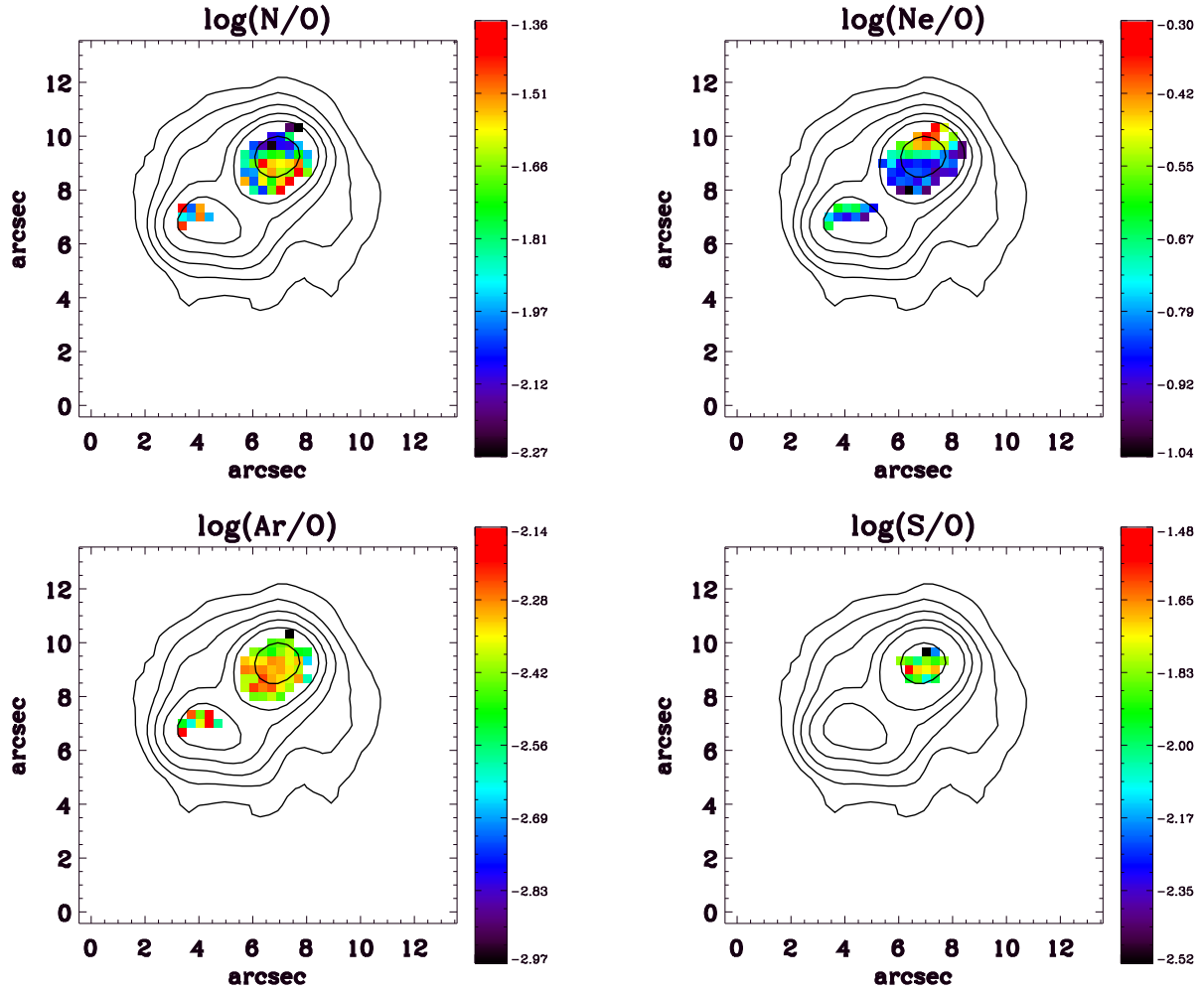


Figure 7. $\log(N/O)$, $\log(Ne/O)$, $\log(Ar/O)$ and $\log(S/O)$ abundance maps for Tol 65. H α emission line contours are overlaid in the panels. North is up and east is to the left.

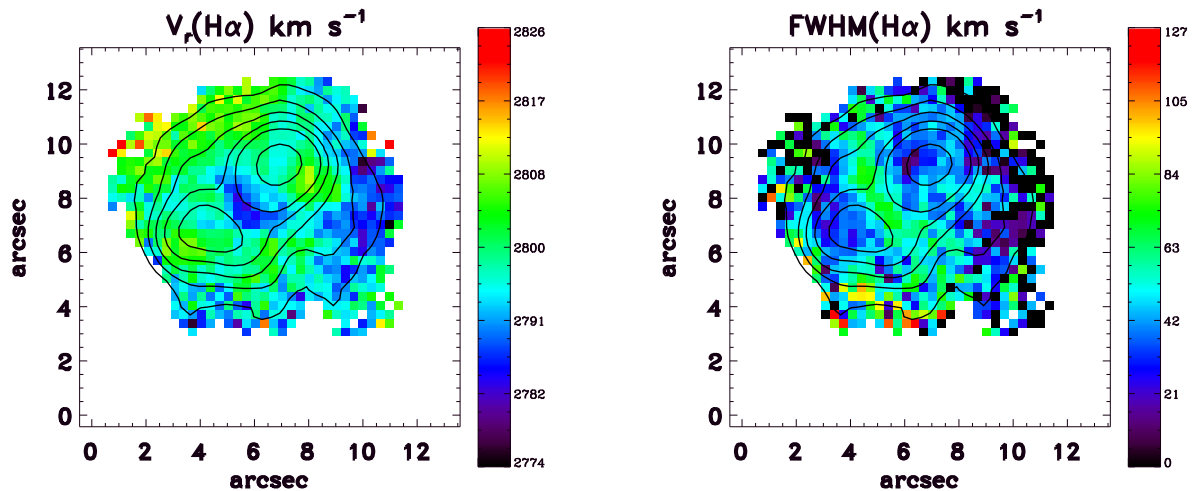


Figure 9. Radial velocity and FWHM maps of the ionized gas obtained from the H α emission line. FWHM corrected by instrumental and thermal broadening. H α emission line contours are overlaid in the panels. North is up and east is to the left.

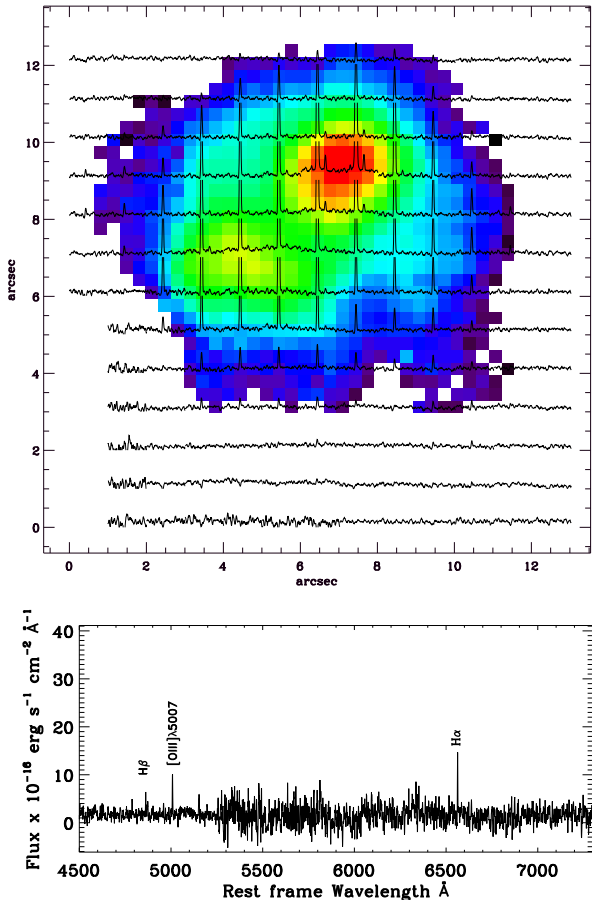


Figure 10. Upper panel: Spatial distribution of the binned ($\sim 1''$ spaxels) $H\alpha$ profiles in the galaxy over the $0.33''$ spaxels. See Sect. 4.2.4. North is up and east is to the left. Lower panel: Integrated spectrum of the tail. From this fig. we observe the presence of an extended nebular emission in the tail of the galaxy.

Table 5. Emission lines and physical properties of the gas in the tail of the galaxy. The fluxes are relative to $F(H\beta)=100$.

	$F(\lambda)/F(H\beta)$	$I(\lambda)/I(H\beta)$
$[OIII] \lambda 5007$	227.38 ± 2.81	222.88 ± 3.90
$H\alpha \lambda 6563$	330.30 ± 7.19	282.14 ± 8.68
$F(H\beta)^a$	$(1.16 \pm 0.01) \times 10^{-15}$	
$c(H\beta)$	0.23	
$EW(H\beta)^b$	7	

^a In units of $\text{erg cm}^{-2} \text{s}^{-1}$

^b \AA

indicator of the amount of material present in this structure. This can be made using the $H\alpha$ emission-line luminosity $L(H\alpha)=7.14 \times 10^{38} \text{ erg s}^{-1}$ and the expression for the mass of the ionized gas from Osterbrock & Ferland (2006);

$$M(HII) = \frac{L(H\alpha)m_p}{n_e \alpha_{H\alpha}^{eff} h\nu_{H\alpha}}, \quad (1)$$

where m_p is the mass of the proton and n_e is the electron density. We use the effective recombination coefficient α^{eff} for $H\alpha$ and case B emission at $T=2 \times 10^4 \text{ K}$ (Osterbrock & Ferland 2006). Thus, assuming an average electron density of $\sim 10 \text{ cm}^{-3}$, we find a total mass of ionized hydrogen in the tail of $M(HII) \sim 1.70 \times 10^5 M_\odot$. This mass corresponds with ~ 24 per cent of the total ionized mass¹ of the galaxy (or ~ 3 per cent if we consider $\sim 100 \text{ cm}^{-3}$) with $M(HII) \sim 7.00 \times 10^5 M_\odot$. Although this mass estimate is approximate, it could clearly indicate that there is a large amount of $H I$ in this extended structure.

5 DISCUSSION

5.1 Star-formation rate and metallicity

The star-formation rate (SFR) inferred using the Kennicutt (1998) formula after correction for a Kroupa IMF (Calzetti et al. 2007), is $0.152 M_\odot \text{ yr}^{-1}$ for the main body of the galaxy and $0.090 M_\odot \text{ yr}^{-1}$ and $0.016 M_\odot \text{ yr}^{-1}$ for regions nos. 1 and 2, respectively. This global SFRs are low in absolute terms. However, its starbursting nature appears when one computes the specific SFR, i.e. the SFR per unit of mass. Somewhat equivalently, their SFR per unit of area (Σ_{SFR}). We can translate the integrated SFR of the main body into an integrated Σ_{SFR} assuming an aperture of $\sim 1.95 \text{ Kpc}^2$ that corresponds to the total area of this region. Thus, we obtain that $\Sigma_{SFR, body} \simeq 0.078 M_\odot \text{ yr}^{-1} \text{ kpc}^{-2}$. If we compare this result with the one obtained in our previously analyzed XMP BCD galaxy, using IFU spectroscopy, (HS 2236+1344, Lagos et al. 2014) we found that in Tol 65 the Σ_{SFR} is 2 times lower, while the $\Sigma_{SFR, body}$ is comparable to the star-formation per unit of area of local tadpole galaxies (Elmegreen et al. 2012). On the other hand, the Σ_{SFR} in Tol 65, and also in HS 2236+1344, is above the SFRs found in “normal” or more metal rich $H II$ /BCD galaxies. From Fig. 15 in López-Sánchez (2010) it is evident that the SFR per unit of area in our XMP galaxies studied so far are higher than the ones found in most of their sample of $H II$ galaxies. This is explained by the high concentration of $H I$ gas found in XMPs (e.g. Ekta & Chengalur 2010b; Filho et al. 2013).

Using the results obtained in Sect. 4.2.2 we show, in Fig. 11, the spatially resolved relation between the Σ_{SFR} and the oxygen abundance $12+\log(O/H)$ in Tol 65. Even this relation at spaxel scales is dubious, our findings show a marginal anticorrelation between these quantities in the sense that high spatial star-formation is found in regions of lower metallicities (see the linear fit to this relation in Fig 11). The calculation of Pearson’s correlation for these

¹ We used the total $H\alpha$ flux of the galaxy summing all the spaxels over the FoV. Thus, $F(H\alpha)/F(H\beta)=3.4899$ with $F(H\beta)=47.48 \times 10^{-15} \text{ erg cm}^{-2} \text{ s}^{-1}$.

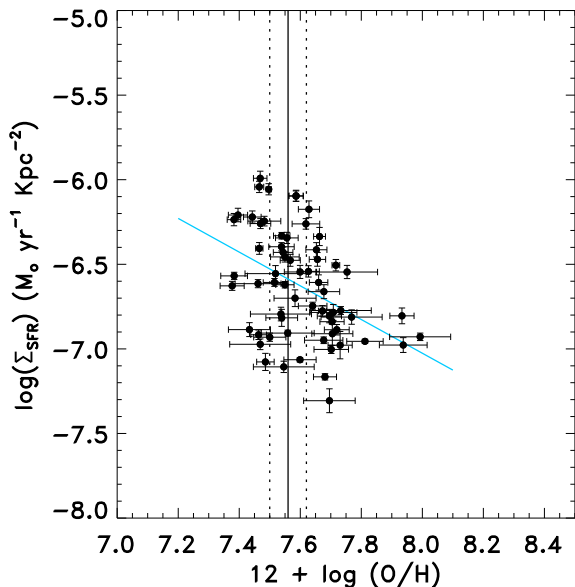


Figure 11. Relation between the star-formation rate surface density Σ_{SFR} and oxygen abundance $12+\log(\text{O}/\text{H})$ at spaxel scales. The cyan line represents the linear fit to this relation. The $12+\log(\text{O}/\text{H})=7.56$ obtained in the main body of the galaxy is represented by the continuous line, while the errors at 1σ level are in dotted lines.

data gives a value of -0.41 , that indicate a moderate monotonically decreasing relationship between these quantities. If we interpret this result as the consequence of an ongoing infall of metal-poor gas from the outskirts the scatter ($\sigma_{(\text{O}/\text{H})}=0.13$ dex) in Fig. 11 clearly indicates that the metals in the ISM are almost fully diluted. Therefore, from an statistical point of view the ISM of the galaxy can be considered chemically homogeneous. We will come back on this discussion later in Sect. 5.4.

5.2 Relation between the starburst activity and the Ly α absorption

It is however worth noting that the age ($\sim 3\text{-}5$ Myr; see Sect. 4.1) of the current burst of Tol 65 agrees with the idea proposed by Thuan & Izotov (1997), in the sense that this galaxy is a young starburst embedded in a static H I cloud, which produces a damped Ly α absorption. Thuan & Izotov (1997) found even with the poor quality of their spectrum, that the O I $\lambda 1302$ absorption line in Tol 65 is blue shifted by ~ 200 km s^{-1} with respect to the emission lines and the Si II $\lambda 1304$ absorption line. They argue that if this is true, the O I absorption would be produced in gas shells moving outward from the central star clusters (Lequeux et al. 1995; Kunth et al. 1998). The spatial distribution of electron density $n_e(\text{S II})$, in Fig. 5, shows a clear area of constant values in region no. 1 with $n_e(\text{S II})\sim 200$ cm^{-3} surrounded by relatively higher density values >200 cm^{-3} . In particular, the area in between the two regions shows spaxels which reach values of $n_e(\text{S II})\sim 500$ cm^{-3} and the $[\text{S II}]\lambda\lambda 6717, 6731/\text{H}\alpha$ ratio (see Fig. 4) is slightly enhanced in this inter-cluster region which would be consistent with an enhanced contribution to the

ionization/excitation by shocks. Therefore, the gas ejected by massive stars within the star clusters grows close to the centre creating a high density region at the same time that the gas expands with velocities close or higher than the supersonic values (with $\sigma > 10$ km s^{-1}) into the surrounding region, then compressing the gas into high-density condensations and creating a low density region between the centre and the expanding high density shells. We found high FWHM values in the same area of high electron density in between the GH IIRs (see Fig. 9) indicating that the turbulent motions in the ionized gas could be produced by winds from the main star cluster complexes. Likewise, the expanding gas would cause the expansion in the surrounding material (H I), so moving it out of the galactic plane. This agrees with the arguments proposed by Thuan & Izotov (1997) and the evolutionary models by Tenorio-Tagle et al. (1999) in order to produce a damped Ly α absorption. In addition, if the wind material contains enough dust, this outflow of gas would give rise to blueshifted velocities (compared to the clusters) observed in between the GH IIRs because redshifted emission would be preferentially extinguished by the dust. In fact, the lack of Ly α emission (see Fig. 2 in Atek et al. 2008) and the detection of relatively high $c(\text{H}\beta)$ associated with the most intense star-forming region in this galaxy, region no. 1, suggest that the Ly α photons have likely been destroyed by dust. This is in good agreement with previous findings by Atek et al. (2008) in the sense that dust extinction is an important Ly α escape regulator.

5.3 The cometary morphology of Tol 65

5.3.1 Feedback from the star-formation activity

A number of recent studies (e.g. Papaderos et al. 2008; Elmegreen & Elmegreen 2010; Elmegreen et al. 2012) have suggested that local galaxies with cometary or tadpole morphology could have a variety of origins. Elmegreen et al. (2012) suggest that most local tadpoles are bulge-free galaxy disks with lopsided star-formation, likely from environmental effects (e.g. ram pressure, disk impacts or random collapse of local disk gas with an unstable Jeans length). Alternatively, propagating star-formation along the tail has been proposed by Papaderos et al. (2008) as one of the mechanisms that lead to the formation of the elongated underlying component or stellar tail of cometary H II/BCDs. Given that the starburst produces enough energy from stellar winds and supernovae (SNe), could the stellar feedback from the starburst have created the stellar tail in this galaxy?

To create a ~ 1.5 kpc long extension in ~ 5 Myr (age of the current burst) would require an outflow velocity ~ 293 km s^{-1} , while the difference between the velocities found in the field is ~ 50 km s^{-1} . Therefore, the current star-formation activity appears to be too young to have pulled out the surrounding gas and stars, driven a galactic outflow, to form the tail. On the other hand, if the global starburst take longer $\sim 10^8$ yr (e.g. McQuinn et al. 2009) as compared to the current burst, certainly it may promote the formation of gas outflows. After that some part of the gas could decelerate and collapse to form the stellar tail. If so, the close similarity between σ_{body} and σ_{tail} agrees with this scenario, given that the diffuse gas will acquire the kinematical information of the system which is transferred into the ISM by the star-

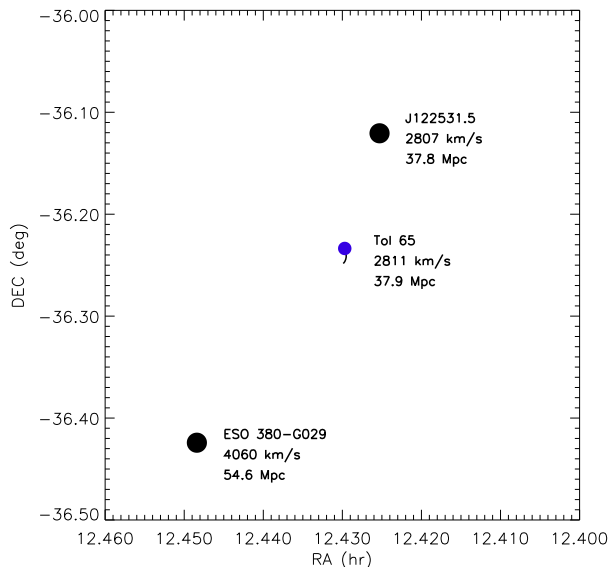


Figure 12. Field on the plane of the sky of Tol 65 (blue dot). We indicate in black the galaxies ESO 380-G029 (SB(s)m) and GALEXMSC J122531.50-360715.3 (Irr). In this figure we show for each galaxy the heliocentric velocity and the distance (3K CMB) obtained from NED.

formation activity (e.g. Moiseev, Tikhonov & Klypin 2015). Papaderos et al. (1999) found that the relatively red colors of the underlying stellar component, in Tol 65, suggest a stellar population with a mean age of $\lesssim 1$ Gyr. This stellar age is compatible with this idea, but the intrinsic youth of XMPs is questionable (Papaderos et al. 2008) and the evidence of such strong winds and the presence of extended ($\gtrsim 1$ kpc) super-shells in low luminosity dwarf galaxies is also sparse. Finally, we did not observe evidences of propagating star-formation along the galaxy and the presence of star clusters in the tail. Thus, there seems to be no correlation between the star-forming activity and the formation of the tail in this galaxy, but from our present data we cannot rule out completely this possibility.

5.3.2 Tidal interactions, mergers and/or gas infall

In many respects, the tidal hypothesis is an attractive one for the origin of the tail in Tol 65, given that tidal interactions enhance lopsidedness in low mass galaxies (Yozin & Bekki 2014). However, HII/BCDs tend to populate low-density environments and are not associated with massive galaxies (e.g. Telles & Terlevich 1995; Telles & Maddox 2000; Noeske et al. 2001) suggesting that tidal interactions with massive companions could not be the dominant starburst triggering mechanism. Thus, the cometary or tadpole shapes among these may not generally be major mergers. We used the NASA/IPAC Extragalactic Database (NED) to search for nearby objects with measured systemic velocities. Figure 12 shows the field on the plane of the sky of the galaxy. We find two galaxies, with measured velocities, in the field of Tol 65. The first one J122531.50-360715.3 is an irregular (dIrr) and likely dwarf galaxy with a difference between their respective systemic velocities of $\Delta V = -4$ km s $^{-1}$. ESO

Digitized Sky Survey (DSS) images show that this object is highly disturbed with an apparent size of $\sim 30''$ equivalent with ~ 6.2 kpc, which is two times the apparent size of Tol 65. The projected distance between these galaxies is $r_p \sim 100$ kpc. The other object in the field is the spiral galaxy ESO 380-G029. For this galaxy we found a $\Delta V = 1249$ km s $^{-1}$, thus it is unlikely that this galaxy is producing the tidally-disturbed tail present in the galaxy, because companions with $\Delta V > 500$ km s $^{-1}$ have not a significant dynamical influence (Noeske et al. 2001). It is interesting to note that the tail of the galaxy is oriented, in the plane of the sky, to this spiral galaxy. Possibly ESO 380-G029 had a stronger influence over Tol 65 in the past (several Gyr ago), thus the tail in the latter could be a remnant of that tidal interaction. However, there is no observational evidence showing that this galaxy had an interaction in the past with Tol 65 to produce a tidal tail. Papaderos et al. (1999) using VLT images suggested the presence of a low-surface-brightness companion galaxy of Tol 65, but it was discarded by Izotov et al. (2004). They found this object is in fact a background galaxy. Thus, if this extended structure has a tidal origin with a close companion(s) it may be related with a faint and massive one that have not been identified by optical surveys. In any case, J122531.50-360715.3 remains as the only potential perturber. In this sense, the slight enhancement of the SFR in region no. 1 with respect to region no. 2 and the lopsidedness of those star-forming regions could be the consequence of this tidal interaction. Although it is unlikely that another dwarf galaxy of low mass, as it seems, could have a tidal effect at this distance. From the present observations we cannot say much about the impact of J122531.50-360715.3 over the physical properties of Tol 65 but we speculate based on the aforementioned arguments that the co-evolution on these systems play an important role in the enhancement of star-formation (e.g. Stierwalt et al. 2014) and evolution in many of these galaxies (Papaderos 2012).

Several studies have shown that a number of star-forming dwarf galaxies present filamentary H I and/or extended structures, which may indicate a recent cold gas infall/accretion (e.g. Ekta, Chengalur & Pustilnik 2008; Ekta & Chengalur 2010a; Lelli, Verheijen & Fraternali 2014) and/or minor merger/interaction (e.g. Martínez-Delgado et al. 2012; Chengalur et al. 2015). In this sense, the extended structure of this galaxy could be a remnant of one of these processes. Verbeke et al. (2014) argue that if the stars are being formed as a consequence of the infall they will be formed along the path of the accretion. But, we did not observe the presence of star clusters in the tail of the galaxy. Then, alternatively, the effect of these interactions has carried away in the recent past an important fraction of gas and stars to form the stellar tail. The fact that $\sigma_{HII, body} \simeq \sigma_{HII, tail} \simeq \sigma_{HI}$ (see Sect. 4.3) implies that the ionized gas still, on a global scale, retains the kinematic memory of its parental cloud and likely a common origin. While extended regions of diffuse gas are highly disturbed, probably due to unresolved expanding shells and the effects of massive star evolution. Therefore, we interpreted the observed properties of the ISM and the morphology of the galaxy as due to a late-stage minor merger and/or inflow of metal-poor gas in the recent past of the galaxy.

5.4 On the metallicity of the ISM

If the current star-forming episode in XMPs is the consequence of the infall of metal-poor gas, the less enriched gas dilutes the preexisting nuclear gas to produce a lower metallicity than would be obtained prior to the accretion. Filho et al. (2015) argue that such accretion flows could explain all the major XMP properties such as, i.e., isolation, lack of interaction/merger signatures, metal-poor H I gas, metallicity inhomogeneities, etc. In this sense, Sánchez Almeida et al. (2014a) argue that the variation of oxygen abundance along the major axis of two XMP star-forming dwarf galaxies can be interpreted as an early stage of assembling in disk galaxies with the star-formation sustained by external metal-poor gas accretion likely from the cosmic web (Sánchez Almeida et al. 2014b). In Lagos et al. (2014) we studied one of the objects analyzed by Sánchez Almeida et al. (2014a), the XMP galaxy HS 2236+1344. In this study, we found indications of variation of O and N/O associated with the less luminous star-formation region of that galaxy. But given the uncertainties related to those measurements we considered the abundances across the galaxy as fairly uniform. Since most of our H II/BCD galaxies (Lagos et al. 2009, 2012, 2014), and XMP/BCDs from the literature (Lagos & Papaderos 2013, see references therein) studied so far are chemically homogeneous it seems that these galaxies have mixed up the metals with the pre-existing ISM before the current starburst appears. The newly synthesized metals from the current star-formation episode reside in a hot gas phase ($T \gtrsim 10^6$ K) and those will be dispersed probably in the whole galaxy by the expansion of starburst-driven outflows. The energy injected by stellar winds and SNe may be able to eject part of the enriched gas into the intergalactic medium, but in most cases the expanding velocity (e.g. van Eymeren et al. 2010, and references therein) are not sufficient to allow the gas to escape from the potential well of the galaxies. In addition, inflows or accretion of relatively low metallicity gas could possibly dilute more easily the abundance of the gas on large scales. Assuming a sound speed of ~ 12 km s $^{-1}$ (see Sect. 4.3) as the expected speed at which mixing occurs in Tol 65, we found that over 1.5-2.0 kpc it yields $\sim 10^8$ yr, which is similar to the timescale required for cooling and dispersal of metals produced by massive stars (e.g. Tenorio-Tagle 1996) as observed in compact H II/BCD galaxies (e.g. UM 408; Lagos et al. 2009). Consequently, the predominant mechanism for metal transport may not be resolved in star-forming dwarf galaxies. However, if we interpreted the observed properties of the ISM as due to a late stage-merger and/or inflow of metal-poor gas, the accreted gas must be almost fully diluted as seen in Fig. 11. Therefore, the final mixture of gas thus depends on the relative enrichment of the acquired and pre-enriched gas.

Lebouteiller et al. (2009) showed that the neutral gas metallicity, in a sample of BCDs, is equal or lower than the ones found in the H II region. This agrees with the results obtained by Lebouteiller et al. (2013), using the Cosmic Origin Spectrograph (COS) onboard HST, in the sense that the H I gas abundances is factor ~ 2 lower than the warm gas abundance in I Zw 18 indicating that infall of, non fully pristine, metal-poor gas could be the responsible for its low metallicity. Therefore, we cannot exclude that the tail in this XMP

galaxy could be made from a gas with much lower metallicity than that in the warm gas phase. However, we still lack an adequate explanation about the evolutionary status of Tol 65 since no spatially resolved H I observations are available, but the infall/accretion of cold gas from the outskirts of the galaxy and/or minor merger/interaction with a small companion recently in the past of the galaxy could explain the main properties of the galaxy. As mentioned above, the tail and the *cometary morphology* could be the remnant of these interactions in which an appreciable fraction of gas has been carried away as the result of the tidal torques, then producing the mixing of metals through the ISM at large scales. In this sense, the scatter in Fig. 11 indicates that the metals in the ISM were diluted in a relatively small timescale. If the past infall of metal poor gas do not explain the low metallicity of Tol 65, alternatively, it could be merely a consequence of the low star-formation efficiency due by the cosmic downsizing.

6 SUMMARY AND CONCLUSIONS

In this work we have presented VIMOS-IFU spectroscopy of the XMP H II/BCD galaxy Tol 65. We studied the spatial distribution of properties (i.e., emission lines, abundances, kinematics, etc) through the ISM of the galaxy in an extended area of $13'' \times 13''$ encompassing the two GH IIRs and most of the extended stellar tail. Below, we summarize our results and conclusions:

(i) This galaxy shows a clear cometary shape with a bright main body and an extended and diffuse stellar tail. We found that the current star-formation activity in Tol 65 started recently about 3-5 Myr ago. Our observations show the presence of an extended H α emission in the tail of the galaxy. The mass of the ionized gas in the tail corresponds to ~ 24 per cent of the total mass of the ionized gas in the galaxy.

(ii) The integrated properties in the main body of the galaxy, it to say, the extinction coefficient $c(H\beta)=0.29$, oxygen abundance $12+\log(O/H)=7.56\pm 0.06$, velocity dispersion $\sigma=20.8\pm 0.6$ kms $^{-1}$ obtained in this study agree, within the uncertainties, with the ones determined in the literature (e.g. Kunth & Sargent 1983; Izotov et al. 2004; Guseva et al. 2011; Bordalo & Telles 2011).

(iii) The velocity field V_r in Tol 65 is highly disturbed and it shows no global rotation pattern. We found $\sigma_{HII,body} \simeq \sigma_{HII,tail} \simeq \sigma_{HI}$ suggesting that the gas still retains the kinematic memory of its parental cloud and a common origin. While extended regions of diffuse gas are highly disturbed, probably due to unresolved expanding shells and the effects of massive star evolution.

(iv) We did not observe a spatial variation of metal (O, N, Ne, Ar and S) in the ISM of the galaxy. This agrees with previous observations in other H II galaxies in the literature (Lagos & Papaderos 2013, and references therein). Although the evidence is far from conclusive, we favour the idea that the most likely mechanisms to produce the flat abundance gradient and the cometary morphology in this XMP H II/BCD is the infall/accretion of cold gas from the outskirts of the galaxy or minor

merger/interaction with an small companion recently in the past of the galaxy. This is in agreement with the scatter found between the gas metallicity ($12+\log(\text{O}/\text{H})$) and star-formation rate at spaxel scales, in Fig. 11, which clearly indicates that the metals in the ISM are almost fully diluted.

Our VIMOS-IFU observation of Tol 65 provides a picture in which a late-stage minor merger and/or infall of gas explain most of the observed properties over the ISM. Therefore, we suggest that these global effects might be attributed as the main mechanism diminishing the preexisting metal of the galaxy (e.g. Leboutteiller et al. 2013), then keeping the oxygen abundance (and other α elements) constant through the ISM at large scales. Clearly, H I observations of Tol 65 with high spatial resolution and HST COS observations are needed in order to study the cool gas component and check whether the proposed mechanism are capable to produce the homogeneity of the ISM, the difference between the neutral and warm gas metallicity and the morphology of this XMP galaxy.

ACKNOWLEDGMENTS

We would like to thank the referee, Dr. Daniel Kunth, for his very valuable comments and suggestions. This work was supported by Fundação para a Ciência e a Tecnologia (FCT) through the research grant UID/FIS/04434/2013. P.L. is supported by a Post-Doctoral grant SFRH/BPD/72308/2010, funded by FCT (Portugal). R.D. gratefully acknowledges the support provided by the BASAL Center for Astrophysics and Associated Technologies (CATA), and by FONDECYT grant N. 1130528. P.L., P.P., A.H., N.R. and J.M.G. acknowledge support by the FCT under project FCOMP-01-0124-FEDER-029170 (Reference FCT PTDC/FIS-AST/3214/2012), funded by the FEDER program. P.P. is supported by FCT through the Investigador FCT Contract No. IF/01220/2013 and POPH/FSE (EC) by FEDER funding through the program COMPETE. J.M.G. is supported by a Postdoctoral grant SFRH/BPD/66958/2009, funded by FCT (Portugal). We acknowledge support by the exchange programme Study of Emission-Line Galaxies with Integral- Field Spectroscopy (SELGIFS, FP7-PEOPLE-2013-IRSES-612701), funded by the EU through the IRSES scheme. This research has made use of the NASA/IPAC Extragalactic Database (NED) which is operated by the Jet Propulsion Laboratory, California Institute of Technology, under contract with the National Aeronautics and Space Administration.

REFERENCES

- Atek, H., Kunth, D., Hayes, M. Östlin, G., Mas-Hesse, J. M. 2008, *A&A*, 488, 491
- Baldwin, J. A., Phillips, M. M., Terlevich R. 1981, *PASP*, 93, 5
- Bekki, K. 2008, *MNRAS*, 388, 10
- Bordalo, V., Telles, E. 2011, *ApJ*, 735, 52
- Bordalo, V., Plana, H., Telles E. 2009, *ApJ*, 696, 1668
- Bournaud, F., Elmegreen, B. G. 2009, *ApJ*, 694, 158
- Cardelli, J. A., Clayton, G. C., Mathis, J. S. 1989, *ApJ*, 345, 245
- Calzetti, D. et al. 2007, *ApJ*, 666, 870
- Cerviño, M., Mas-Hesse, J. M. 1994, *A&A*, 284, 749
- Copetti, M. V. F., Pastoriza, M. G., Dottori, H. A. 1986, *A&A*, 156, 111
- Charlot, S., Fall, S. M. 1993, *ApJ*, 415, 580
- Chengalur, J. N., Pustilnik, S. A., Makarov, D. I., Perepelitsyna, Y. A., Safonova, E. S., Karachentsev, I. D. 2015, *MNRAS*, 448, 1634
- Dekel, A., Birnboim, Y. 2006, *MNRAS*, 368, 2
- Dekel, A., Birnboim, Y., Engel, G., Freundlich, J., Goerdt, T., Mumcuoglu, M., et al. 2009, *Nature*, 457, 451
- De Robertis, M. M., Dufour, R. J., Hunt, R. W. 1987, *JRASC*, 81, 195
- Dottori, H. A. 1981, *Ap&SS*, 80, 267
- Duc, P.-A., Bournaud, F., Masset, F. 2004, *A&A*, 427, 803
- Duc, P.-A., Cuillandre, J.-C., Serra, P., et al. 2011, *MNRAS*, 417, 863
- Ekta, B., Chengalur, J. N. 2010a, *MNRAS*, 403, 295
- Ekta, B., Chengalur, J. N. 2010b, *MNRAS*, 406, 1238
- Ekta, B., Chengalur, J. N., Pustilnik, S. A. 2008, *MNRAS*, 391, 881
- Elmegreen, B. G., Elmegreen, D. M. 2010 *ApJ*, 722,1895
- Elmegreen, D. M., Elmegreen, B. G., Sánchez Almeida, J., Muñoz-Tuñón, C., Putko, J., Dewberry, J. 2012, *ApJ*, 750, 95
- Filho, M. E., Winkel, B., Sánchez Almeida, J., Aguerri, J. A., Amorín, R., Ascasibar, Y., Elmegreen, B. G., Elmegreen, D. M., Gomes, J. M., Humphrey, A., Lagos, P., Morales-Luis, A. B., Muñoz-Tuñón, C., Papaderos, P., Víchez, J. M. 2013, *A&A*, 558, 18
- Filho, M. E., Sánchez Almeida, J., Muñoz-Tuñón, C., Nuza, S. E., Kitaura, F., Hess, S. 2015, *ApJ*, 802, 82
- Giavalisco, M., Koratkar, A., Calzetti, D. 1996, *ApJ*, 466, 831
- Gil de Paz, A., Madore, B. F., Pevunova, O. 2003, *ApJS*, 147, 29
- Guaita, L., Melinder, J., Hayes, M., et al. 2015, *ApJ*, 576, A51
- Guseva, N. G., Izotov, Y. I., Stasinska, G., Fricke, K. J., Henkel, C., Papaderos, P. 2011, *A&A* 529, 149
- Guseva, N. G., Izotov, Y. I., Fricke, K. J., Henkel, C. 2012, *A&A*, 541, 115
- Humphrey, A., Vernet J., Villar-Martín, M., di Serego Alighieri, S., Fosbury, R. A. E., Cimatti, A., 2013, *ApJ*, 768, L
- Izotov, Y. I., Lipovetsky, V. A., Chaffee, F.H., Foltz, C. B., Guseva, N. G., Kniazev, A. Y. 1997, *ApJ*, 476, 698
- Izotov, Y. I., Papaderos, P., Guseva, N. G., Fricke, K. J., Thuan, T. X. 2001, Izotov, Y. I., Chaffee, F. H., Green, R. F. 2001, *ApJ*, 562, 727
- Izotov, Y. I., Papaderos, P., Guseva, N. G., Fricke, K. J., Thuan, T. X. 2004, *A&A*, 421, 539
- Izotov, Y. I., Schaerer, D., Blecha, A., Royer, F., Guseva, N. G., North, P. 2006, *A&A*, 459, 71
- Kennicutt, R. C. 1998 *ARA&A*, 36, 189
- Kingsburgh, R. L., Barlow, M. J. 1994, *MNRAS*, 271, 257
- Kobulnicky, H. A., Skillman, E. D. 1997, *ApJ*, 489, 636
- Kobulnicky, H. A., Skillman, E. D. 1998, *ApJ*, 497, 601
- Kunth, D., Sargent, W. L. W. 1983, *ApJ*, 273, 81
- Kunth, D., Joubert, M. 1985, *A&A*,142, 411

- Kunth, D., Lequeux, J., Sargent, W. L. W., Viallefond, F. 1994, *A&A*, 282, 709
- Kunth, D., Mas-Hesse, J. M., Terlevich, E., Terlevich, R., Lequeux, J., Fall, S. M. 1998, *A&A*, 334, 11
- Kunth, D., Östlin, G. 2000, *ARA&A*, 10, 1
- Lagerholm, C., Kuntschner, H., Cappellari, M., Krajinovic, D., McDermid, R. M., Rejkuba, M. 2012, *A&A*, 541, 82
- Lagos, P., Telles, E., Melnick, J. 2007, *A&A*, 476, 89
- Lagos, P., Telles, E., Muñoz-Tuñón, C., Carrasco, E. R., Cuisinier, F., Tenorio-Tagle, G. 2009, *AJ*, 137, 5068
- Lagos, P., Telles, E., Nigoche-Netro, A., Carrasco, E. R. 2011, *AJ*, 142, 162
- Lagos, P., Telles, E., Nigoche-Netro, A., Carrasco, E. R. 2012, *MNRAS*, 427, 740
- Lagos, P., Papaderos, P. 2013, *AdAst*, 2013, 20
- Lagos, P., Papaderos, P., Gomes, J. M., Smith, A. V., Vega, L. R. 2014, *A&A*, 569, 110
- Lebouteiller, V., Heap, S., Hubeny, I., Kunth, D. 2009, *A&A*, 494, 915
- Lebouteiller, V., Heap, S., Hubeny, I., Kunth, D. 2013, *A&A*, 553, 16
- Lequeux, J., Kunth, D., Mas-Hesse, J. M., Sargent, W. L. W. 1995, *A&A*, 301, 18
- Lee, H., Skillman, E. D. 2004, *ApJ*, 614, 698
- Leitherer, C., et al. 1999, *ApJS*, 123, 3
- Lelli, F., Verheijen, M., Fraternali, F. 2014, *MNRAS*, 445, 1694
- Loose, H.-H., Thuan, T. X. 1986, *ApJ*, 309, 59
- López-Sánchez, Á. R. 2010, *A&A*, 521, 63
- Martínez-Delgado, D., Romanowsky, A. J., Gabany, R. J., et al. 2012, *ApJ*, 748, 24
- McQuinn, K. B. W., Skillman, E. D., Cannon, J. M., Dalcanton, J. J., Dolphin, A., Stark, D., Weisz, D. 2009, *ApJ*, 695, 561
- Moiseev, A. V., Tikhonov, A. V., Klypin, A. 2015, *MNRAS*, 449, 3568
- Noeske, K. G., Iglesias-Páramo, J., Vilchez, J. M., Papaderos, P., Fricke, K. J. 2001, *A&A*, 371, 806
- Noeske, K. G., Papaderos, P., Cairós, L. M., Fricke, K. J. 2003, *A&A*, 410, 481
- Osterbrock, D. E., Ferland, G. J. 2006, *Astrophysics of gaseous nebulae and active galactic nuclei*, 2nd. edn. (Sausalito, CA: University Science Books)
- Papaderos, P., Fricke, K. J., Thuan, T. X., Izotov, Y. I., Nicklas, H. 1999, *A&A*, 352, 57
- Papaderos, P., Guseva, N. G., Izotov, Y. I., Fricke, K. J. 2008, *A&A*, 491, 113
- Papaderos, P., Östlin, G. 2012, *A&A*, 537, A126
- Papaderos, P. 2012, in *Dwarf Galaxies: Keys to Galaxy Formation and Evolution*, proceedings of JENAM 2010 (Lisbon, September 2010), P. Papaderos, S. Recchi, G. Hensler (eds.), Springer Verlag, p. 321
- Papaderos, P., Gomes, J. M., Vilchez, J. M. et al. 2013, *A&A Letters*, 555, 1
- Pagel, B. E. J., Simonson, E. A., Terlevich, R. J., Edmunds, M. G. 1992, *MNRAS*, 255, 325
- Partridge, R. B., Peebles, P. J. E. 1967, *ApJ*, 147, 868
- Pérez-Montero, E., Vilchez, J. M., Cedrés, B., Hägele, G. F., Mollá, M., Kehrig, C., Díaz, A. I., García-Benito, R., Martín-Gordón, D. 2011, *A&A*, 532, 141
- Pustilnik, S. A., Martin, J.-M. 2007, *A&A*, 464, 859
- Pustilnik, S. A., Kniazev, A. Y., Lipovetsky, V. A., Ugryumov, A. V. 2001, *A&A*, 373, 24
- Rich, J. A., Torrey, P., Kewley, L. J., Dopita, M. A., Rupke, D. S. N. 2012, *ApJ*, 753, 5
- Roy, J.-R., Kunth, D. 1995, *A&A*, 294, 432
- Rupke, D. S. N., Kewley, L. J., Barnes, J. E. 2010, *ApJ*, 710, 156
- Shaw, R. A., Dufour, R. J. 1994, *ASPC*, 61, 327
- Sanders, D. B., Soifer, B. T., Elias, J. H., et al. 1988, *ApJ*, 325, 74
- Sánchez Almeida, J., Muñoz-Tuñón, C., Elmegreen, D. M., Elmegreen, B. G., Méndez-Abreu, J. 2013, *ApJ*, 767, 74
- Sánchez Almeida, J., Morales-Luis, A. B., Muñoz-Tuñón, C., Elmegreen, D. M., Elmegreen, B. G., Méndez-Abreu, J. 2014a, *ApJ*, 783, 45
- Sánchez Almeida, J., Elmegreen, B. G., Muñoz-Tuñón, C., Elmegreen, D. M. 2014b, *A&ARv*, 22, 71
- Smoker, J. V., Davies, R. D., Axon, D. J., Hummel, E. 2000, *A&A*, 361, 19
- Springel, V. 2000, *MNRAS*, 312, 859
- Stierwalt, S., Besla, G., Patton, D., Johnson, K., Kallivayalil, N., Putman, M., Privon, G., Ross, G. 2015, *ApJ*, 805, 2
- Straughn, A. N., Cohen, S. H., Ryan, R. E., et al. 2006, *ApJ*, 639, 724
- Taylor, C., Brinks, E., Skillman, E. D. 1993, *AJ*, 105, 128
- Telles, E., Terlevich, R. 1995, *MNRAS*, 275, 1
- Telles, E., Maddox, S. 2000, *MNRAS*, 311, 307
- Tenorio-Tagle, G. 1996, *AJ*, 111, 1641
- Tenorio-Tagle, G., Silich, S. A., Kunth, D., Terlevich, E., Terlevich, R. 1999, *MNRAS*, 309, 332
- Thuan, T. X., Izotov, Y. I. 1997, *ApJ*, 489, 623
- Thuan, T. X., Izotov, Y. I., Lipovetsky, V. A. 1997, *ApJ*, 477, 661
- Toomre, A. 1977, *ARA&A*, 15, 437
- van Eymeren, J., Koribalski, B. S., López-Sánchez, Á. R., Dettmar, R.-J., Bomans, D. J. 2010, *MNRAS*, 407, 113
- Verbeke, R., De Rijcke, S., Koleva, M., Cloet-Osselaer, A., Vandenbroucke, B., Schroyen, J. 2014, *MNRAS*, 442, 1830
- Villar-Martín, M., Humphrey, A., De Breuck, C., Fosbury, R., Binette, L., Vernet, J. 2007, *MNRAS*, 375, 1299
- Walsh, J. R., Roy, J. R. 1990, *ESOC*, 34, 95
- Yozin, C., Bekki, K. 2014, *MNRAS*, 439, 1948